SiC Substrate Composition Effect on TGO Scale Growth in EBC Systems During High Temperature Steam Exposure

K. D. Ardrey*, M. J. Lance, M. J. Ridley

Materials Science and Technology Division, Oak Ridge National Laboratory, Oak Ridge, TN 37831, USA

*Corresponding Author**

Dr. Kristyn D. Ardrey, ardreykd@ornl.gov

Keywords: EBC, TGO, SiC, High Temperature Oxidation, Rare-Earth

Abstract

A systematic investigation was conducted on the oxidation behavior of silicon-bond coats within environmental barrier coating (EBC) systems applied to Si-carbide (SiC) substrates, aiming to understand how different underlying SiC substrates influence the bond coat's thermally grown oxide (TGOs) and its properties. The study examined $(Y/Yb)_2Si_2O_7$/Si coatings on three cost-effective surrogate SiC substrates (chemical vapor deposition (CVD) grown β-SiC, sintered α-SiC, and reaction-bonded (RB) SiC), for SiC_{fiber}/SiC_{matrix} ceramic matrix composites (CMCs). Discrepancies in TGO growth were observed, with noticeably higher growth rates reported for the

coated CMC specimens than the four monolithic SiC specimens. The CMC samples produce an amorphous TGO, whereas the other monolithic substrates formed a crystalline TGO, which lowered the oxygen permeability through the SiO_2 scale. The vitrification of the TGO in the $(Y/Yb)_2Si_2O_7$/Si/CMC system resulted from the migration of boron species from the CMC substrate to the SiO_2 scale, leading to network modification via boron doping.

1 Introduction

Combustion turbines have continuously advanced in their efficiency due to both design considerations and increasing turbine inlet temperatures. Primary materials considerations for allowing higher operating temperatures include the incorporation of single crystal superalloys [1], thermal barrier coatings on metallic components [2], and most recently SiC_{fiber}/SiC_{matrix} (SiC/SiC) ceramic matrix composites (CMCs) with environmental barrier coatings (EBCs) [3]. Using SiC/SiC CMCs as superalloy replacements for turbine engine components can potentially provide a higher operating temperature (1200°C–1400°C), lower weight, and increased operating efficiency [4], [5], [6]. However, SiC/SiC CMCs are susceptible to the high-temperature water vapor environments that exist inside of combustion turbine engines during service. The steam environment results in the formation of a SiO_2 thermally grown oxide (TGO) via the reaction in Equation 1. In tandem, the TGO will evaporate due to gaseous hydroxide formation [7], according to Equation 2.

$$SiC + 3H_2O\,(g) = SiO_2 + 3H_2(g) + CO(g) \quad (1)$$

$$SiO_2 + 2H_2O(g) = Si(OH)_4(g) \quad (2)$$

An EBC layer is essential to prevent CMC volatilization and increase component longevity. Currently, leading EBC technology consists of rare earth silicates, such as $Yb_2Si_2O_7$ and

yttrium/ytterbium mixed disilicates creating $(Y/Yb)_2Si_2O_7$, due to their high-temperature stability [8], [9] and similar coefficient of thermal expansion to SiC [10]. EBC systems require a silicon bond coat to enhance coating adhesion and provide an additional oxidation barrier. However, EBC systems can still be susceptible to failure from a multitude of environmental factors, such as molten siliceous debris degradation [11], foreign object damage [12], and interfacial stresses from thermal cycling [13].

Steam oxidation remains a primary failure mode for EBC systems due to relationships between the TGO growth rate and the EBC adhesion strength [14]. While the EBC prevents volatilization, the silicon bond coat is still vulnerable to high-temperature oxidation. Defects within the EBC can create fast diffusion pathways for oxidizing species, making the silicon bond coat layer prone to oxidation. In a high-temperature steam environment, the oxidation of the silicon bond coat intensifies because the solubility of H_2O (g) is three times larger than that of O_2 (g) in high-temperature environments, resulting in thicker a TGO layer [15].

An increasingly thicker TGO layer in high-temperature steam environments can lead to higher interface stresses near the TGO interfaces [16], eventually causing spallation of the protective EBC altogether [17], [18]. The exact mechanism for TGO-involved EBC spallation revolves around interface instability during heating and cooling cycles during service. A phase change from the high-temperature SiO_2 β-cristobalite phase to the low-temperature SiO_2 α-cristobalite phase will occur for a crystalline SiO_2 TGO [17]. Upon cooling, this reversible phase transition from β to α occurs at approximately 250°C and is accompanied by an approximately 5% volume contraction and a change in the linear coefficient of thermal expansion (from ~3×10^{-6} K^{-1} to ~30×10^{-6} K^{-1}) [19], [20]. Over time, thermal cycling can cause stress within the TGO to accumulate due to the β to α phase change transformation; this stress will eventually cause cracks

to form within the SiO_2 scale to alleviate the built-up strain energy at the TGO interfaces [21]. The TGO's built-up stresses and resulting cracking behavior during heating cycles is suspected to cause eventual EBC spallation.

Because TGO growth is a crucial failure mechanism, extensive research has gone into understanding TGO growth kinetics under various conditions for EBC/silicon bond coat systems for SiC/SiC CMCs [22], [23]. Furthermore, many research efforts have been focused on obtaining data to predict service lifetimes for rare earth silicate coating systems. However, even though uniformity is usually maintained for application and compositions of EBC/silicon bond coats of interest, the research space still includes variation in the usage of different SiC substrates that are utilized for coating testing. The reason behind this variation is commonly the relatively high cost of SiC/SiC CMCs [24]; consequently, alternative monolithic SiC substrates are chosen to investigate coating technologies at the laboratory scale.

Primarily, the three SiC alternatives that are used for EBC/silicon bond coat research are chemical vapor deposition (CVD)-grown β-SiC (CVD-SiC), sintered α-SiC (Hexoloy), and reaction bonded (RB) SiC (RB-SiC). Each system has been used in public and private research spaces for EBC analyses, even though each has different microstructures and chemistries. Therefore, the extent to which the underlying SiC substrates influence the properties of the silicon bond coat's TGO during high-temperature steam exposures remains an open question.

1.2 SiC substrates utilized in current EBC research

Significant research efforts have been made to elucidate TGO growth kinetics for EBC systems that coat alternative SiC materials. Upon review, oxidation studies have been conducted primarily on EBC-coated CVD-SiC, Hexoloy, and RB-SiC. Primary microstructural and chemical

differences between CVD-SiC, Hexoloy, and RB-SiC are summarized in Table 1, along-side common properties of SiC/SiC CMCs.

Table 1: List of primary microstructural and chemical differences between CVD, Hexoloy, RB-SiC, and SiC/SiC CMCs.

Type	Manufacturing Method	Majority Phase	Properties	Ref.
CVD-SiC	Chemical Vapor Deposition	β-SiC	100% dense and phase pure	[25]
Hexoloy α-SiC	Pressure-less sintering	α-SiC	Porous microstructure contains free carbon and boron carbide sintering additives	[26], [27]
RB-SiC	Reaction bonded SiC	α- or β-SiC, Si	SiC particles within a silicon matrix	[28]
SiC/SiC CMCs	Woven SiC fibers coated with varying compounds and sealed with a CVD-SiC layer	α- or β-SiC, Si	High cost, not commonly used for lab-scale testing, contains sintering additives like carbon, boron carbides, and boron nitrides.	[24], [29]

Oxidation behavior has been shown to be different for varying stand-alone SiC materials, resulting in discrepancies in substrate TGO properties. B. Kowalski and B. Harder [30] observed that Hexoloy when exposed to high-temperature steam exhibited a thicker TGO layer with 24% porosity compared to the TGO formed on CVD-SiC which had around 3% porosity. The authors attributed this effect to outward diffusion of boron compounds in Hexoloy affecting its resulting microstructure. D. Mieskow et al. [31] found significant porosity in Hexoloy's SiO_2 scale when exposed to 1200°C, attributed to CO(g) from carbon compounds that were used as sintering additives. N. Nasiri et al. [32] linked amorphous TGOs on BN-coated CMCs to boron inclusions in the SiO_2 scale. Regarding stand-alone RB-SiC, few studies exist in public literature on its high-temperature oxidation properties, so its oxidation behavior is less understood.

Research on EBC systems applied to SiC substrates with varying additives, such as boron, reveal variations in the behavior of the silicon bond coat's TGO. General Electric (GE) Company (Schenectady, NY) published two patents regarding boron doping into TGO scales of silicon bond coats for EBC systems. One patent [35] describes how adding boron to the EBC or SiC substrate system can prevent TGO scales from crystallizing, reducing TGO layer cracking and minimizing coating spallation. In contrast, the other patent [36] describes methods for preventing boron and other impurities to diffuse towards the silicon bond coat, in order to protect the TGO scale from higher oxidation rates caused by impurity doping. Furthermore, K. N. Lee et al. [33] observed thicker SiO_2 scales in EBC systems on SiC substrates with high boron concentrations, showcasing that the diffusion of boron or boron-containing phases influences TGO growth during high-temperature exposure. Additionally, M. Presby et al. [34] found that boron migration from CMC substrates to the bond coat did in fact accelerate oxygen diffusivity of TGO scales for EBC-coated CMC samples.

In this study, three monolithic SiC archetypes and SiC/SiC CMCs were investigated by systematically exposing them to thermal cycling in flowing steam to assess substrate effects on TGO kinetics. Quantitative chemical analysis was performed for each system to assess impurity as well as dopant effects on the TGO morphology. The results of this work provide a benchmark for comparing laboratory specimen archetypes used across multiple institutions representing baseline performance metrics for EBC/SiC systems used for predicting EBC lifetimes.

2 Procedure

2.1 Materials

Four different SiC substrates were used for the high-temperature oxidation analysis: CVD-SiC (99.99% purity; the Dow Chemical Company), Hexoloy (Saint-Gobain), RB-SiC (Coherent Corp), and SiC/SiC CMC substrates (NASA Glenn Research Center). The SiC fibers (Hi-Nicalon, NGS Advanced Fibers Co., Ltd.) used for the melt infiltrated SiC/SiC CMCs have been coated with a graphitic carbon interphase layer alongside Si–C–B-containing processing aides within the matrix. Additionally, a CVD SiC seal coat was applied onto the CMC coupons, but the CVD process did not coat the entire surface of the CMC due to the CMCs having a relatively high surface roughness (S_A = 88 μm).

Table 2 describes in more detail the SiC specimens used in this research. For simplicity, the four SiC substrates will be hereafter referred to as: CVD, Hexoloy, RB, and CMC throughout this work.

Table 2: Properties for monolithic SiC and CMCs utilized within this work.

Substrate	Description
CVD	β-SiC, chemically and phase pure
Hexoloy	α-SiC, sintered with B and C-containing sintering aids, high porosity ~8%
RB	α-SiC, SiC surrounded by Si-matrix
CMC	β-SiC fibers (w/ C interphase), β-SiC matrix, melt infiltrated, CVD SiC seal coat

Each SiC substrate was coated with an EBC/silicon bond coat layer via air plasma spray (Stony Brook University's Center for Thermal Spray Research). The coatings were deposited onto one face of the coupon for each of the SiC coupons that were made into circular disks of approximately 2 cm diameter by 0.2 cm thickness.

The EBC composition in this study was a $(Y/Yb)_2Si_2O_7$ solid solution, chosen for its dual capability as an EBC and thermal barrier coating with lower thermal conductivity compared to $Yb_2Si_2O_7$ [37]. In addition to the coated specimens, uncoated silicon coupons (99% pure, cut from a wrought plate), also approximately 2 cm diameter by 0.2 cm thickness, were tested for baseline TGO analysis and compared to the coated silicon bond coat specimens.

2.2 Testing parameters

The specimens were exposed to high-temperature steam oxidation via furnace cycle testing. Each coated coupon had an approximately 2 mm diameter hole drilled through it to allow for hanging on the alumina sample holders that are used to automatically raise and lower each specimen in and out of the furnace for the heating and cooling cycles. The exposures involved 1 h hot cycles up to 1350°C, followed by 10 min cooling cycles that allowed the specimens to cool to near room temperature. The temperature of the samples during cyclic exposure were measured by a type-B thermocouple that was placed along the Al_2O_3 sample holders near the specimens. The high-temperature exposures took place in a flowing steam environment composed of 90% H_2O + 10% O_2(g) with a flow rate of 10 cm/s within the furnace reaction tube made of SiC. The various coated SiC samples underwent exposure cycles of 100 h, 300 h, and 500 h.

2.3 Characterization

X-ray diffraction (Rigaku Smartlab) analysis of the coated coupons was performed via a Cu-Kα source (1.54 λ) at 40 kV and 44 mA, with a 2θ scan ranging from 10° to 80° and a step size of 0.01°. Phase analysis was performed with JADE software (MDI Materials Data) equipped with the International Center for Diffraction Data PDF-5+ database [38].

Cross sections of specimens mounted in epoxy were mechanically polished, and the final polishing step used a 0.05 μm colloidal silica suspension. Approximately 10 nm of sputtered carbon coating, and some specimens with 10 nm of sputtered gold coating, was applied to each sample to prevent charging during scanning electron microscopy (SEM). Field-emission SEM (TESCAN Mira 3 FEG-SEM) via backscatter electron (BSE) imaging was performed at 15 keV on baseline and exposed cross-sectioned specimens. Electron probe microanalysis (EPMA) was conducted via a JXA-8200 (JEOL) microprobe, which was equipped with a backscatter detector and five wavelength-dispersive spectrometers (WDS). Quantification of boron was performed using a low accelerating voltage of 5 kV which enhanced the X-ray intensity of light elements. The 500 h exposed CVD sample's TGO and silicon bond coat were used as blank samples without any boron present to remove the spectrometer background. This was done using the commercial software package probe for EPMA. Raman spectroscopy (InVia, Renishaw, Inc.) was performed on post-exposure specimens using a 532 nm Nd-YAG laser with an approximate spot size of 1 μm.

Size of Oxidation Feature Image Analysis (SOFIA) software [39] was employed to measure the growth of the TGO scales on all $(Y/Yb)_2Si_2O_7$ coated SiC substrates using SEM images of the cross-sectioned specimens. Measurements were made near the center of each of the cross-sectioned specimens. For each coated SiC specimen, 10 SEM images were analyzed (view field per micrograph = 277 μm), resulting in approximately 1000 measurements per micrograph and totaling around 10,000 measurements per sample. ImageJ [40] was used for measurements on the stand-alone silicon samples after exposure because the highly defected oxide layer affected the accuracy of SOFIA's results. For each silicon sample, 15 ImageJ measurements per image were taken from 10 SEM micrographs (view field = 277 μm), resulting in a total of 150 measurements

per sample. Additionally, ImageJ was employed for qualitative phase analysis and density measurements of the EBC and TGO layers.

Qualitative porosity analysis of TGOs was also performed using ImageJ on micrographs of all coated SiC specimens. Three images per sample (view field = 55.4 μm) were used for each exposure time. Furthermore, TGO crack measurements were analyzed by ImageJ on four SEM images for each of the $(Y/Yb)_2Si_2O_7$/Si-coated SiC substrates after exposure. The sample imaging area was approximately the same for each sample with a total distance of 0.691 mm along the length of the TGO measured.

3 Results

3.1 Baseline substrate analysis

SEM-BSE analysis was performed on the baseline SiC substrates to examine their microstructures. Figure 1a presents the CVD microstructure, which is dense and homogeneous. Figure 1b shows the microstructure of the Hexoloy specimen having high porosity and relatively small areas consisting of a darker phase contrast. The porosity of the Hexoloy samples was measured to be about 8% using ImageJ analysis of the micrographs. Figure 1c displays the RB substrate featuring a dual-phase microstructure with SiC particulates surrounded by a silicon matrix. Figure 1d depicts the CMC substrate near a fiber tow.

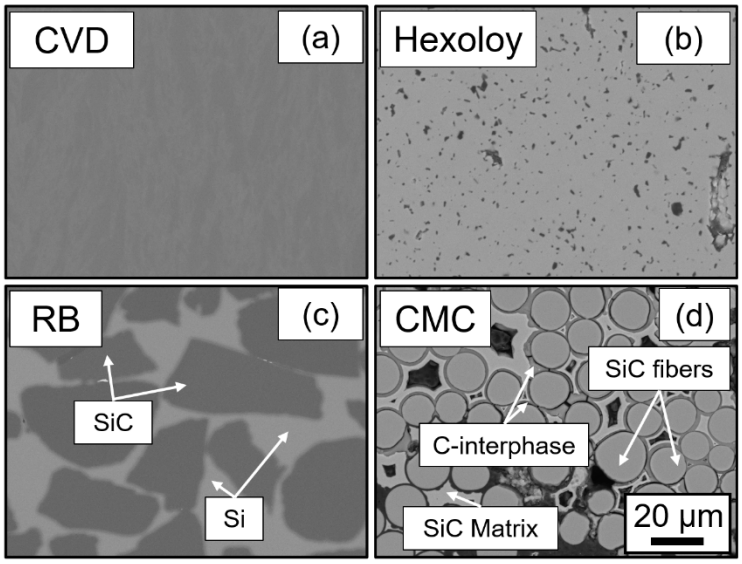

Figure 1: SEM-BSE baseline images of (a) CVD, (b) Hexoloy, (c) RB, and (d) CMC substrates.

Baseline chemical analysis of the unexposed SiC substrates was performed using EPMA, shown in Figure 2. The chemical maps reveal the compositional differences in wt.% among the SiC substrates studied. The Hexoloy and CMC specimens exhibited significant boron content within the substrate. The Hexoloy substrate demonstrated localized boron-rich regions (Figure 2n), suggesting the presence of residual boron compounds after processing. Furthermore, high concentrations of carbon were observed to be scattered throughout the Hexoloy sample (Figure 2r), indicating possible unreacted carbon within the substrate after sintering. Another possibility could be carbon artifacts left over from the polishing process. For the CMC specimen, boron was concentrated around the SiC fiber tows, as shown in Figure 2s. Moreover, concentrations of carbon are shown to be included in the boron rich regions of the CMC specimen.

By contrast, the CVD and RB specimens, shown in Figure 2a and c, did not exhibit significant concentrations of elements other than silicon and carbon (Figure 2i, q, k, s). This EPMA SiC substrate analysis underscores the differences in microstructure and chemical composition,

which may influence the behavior of the EBC system's TGO scale growth under high-temperature conditions.

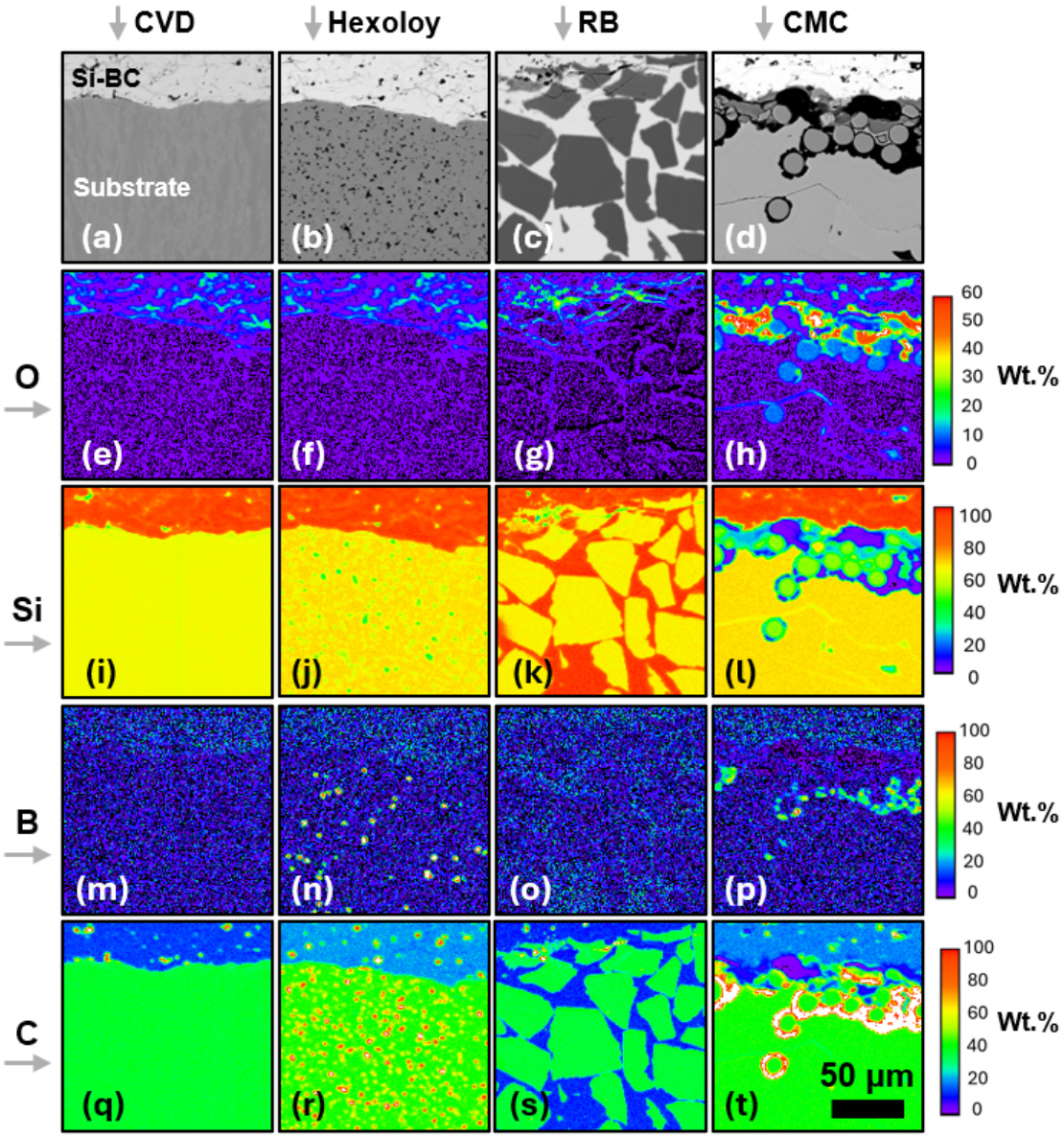

Figure 2: SEM-BSE imaging of (a) CVD, (b) Hexoloy, (c) RB, and (d) CMC. Baseline EPMA elemental map analysis of for all four unexposed SiC substrates for (e-h) O, (i-l) Si, (m-p) B, and (q-t) C in wt.%.

EPMA chemical point analysis (~200 measurements per sample) was conducted to estimate boron content in the baseline CMC and Hexoloy samples. The average boron concentration was 4.0 ± 9.3 wt.% for CMC and 2.3 ± 6.8 wt.% for Hexoloy, with high standard deviations due to non-uniform boron distribution.

3.2 Baseline EBC analysis

SEM-BSE analysis for the EBC/silicon bond coat layer is shown in Figure 3 for each of the coated SiC substrates before exposure. The EBCs were approximately 90%–93% dense, with the other 7% representing pores and cracks. The phase fraction for each of the coatings was about 75% $(Y/Yb)_2Si_2O_7$ and about 25% $(Y/Yb)_2SiO_5$. The phase fraction in the EBC was due to SiO_2 volatility during the air plasma spray process. The silicon bond coat had a density of approximately 98%–99%, with minor cracks and porosity.

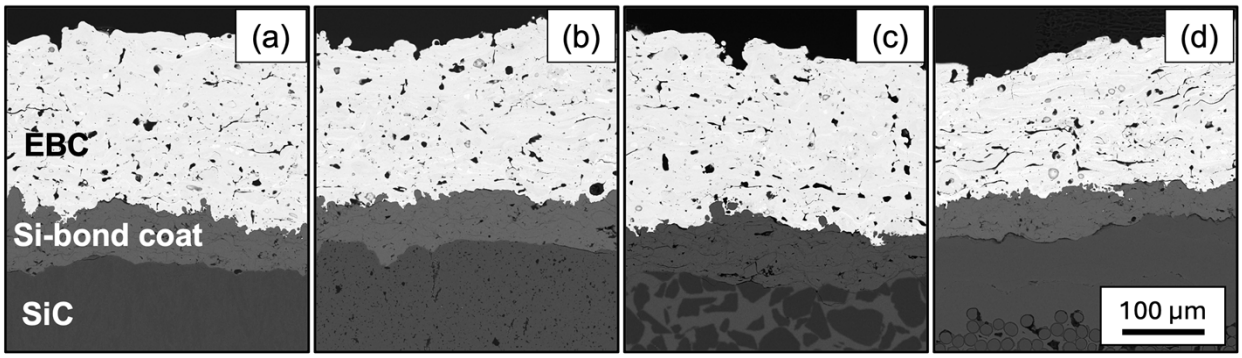

Figure 3: Baseline SEM-BSE analysis of EBCs on varying SiC substrates, (a) CVD, (b) Hexoloy, (c) RB, and (d) CMC.

Table 3 shows the mean, median, standard deviation, and number of measurements (counts) on coating layers for each SiC substrate. The EBC was approximately 200 µm thick, and the silicon bond coat was approximately 58 µm thick. The measurements show that each layer in

the EBC system displays consistent characteristics across all specimens. The average EBC thickness of the CMC specimens is less than that of the other specimens. However, the thickness is within the standard deviation of the other samples.

Table 3: Mean and median thickness measurements via SOFIA for the EBC and silicon bond coat layers from baseline specimens.

SiC Substrate	Coating Layer	Mean Thickness (μm) ± Stdev.	Median Thickness (μm)	Counts
CVD	$(Y/Yb)_2Si_2O_7$	213 ± 15	214	1503
Hexoloy		197 ± 18	194	1489
RB		209 ± 16	209	1475
CMC		190 ± 22	188	1505
CVD	Silicon bond coat	61 ± 11	61	1626
Hexoloy		57 ± 9	57	1668
RB		63 ± 14	64	1517
CMC		55 ± 13	55	1470

3.3 X-ray diffraction analysis

EBC X-ray diffraction characterization was conducted on the EBC/silicon/Hexoloy system in order to gather baseline (0 h exposure) and 500 h exposure at 1350°C analysis, shown in Figure 4. The baseline specimen, seen in Figure 4a, consisted of $(Y/Yb)_2Si_2O_7$ and a minor phase of $(Y/Yb)_2SiO_5$. After steam furnace cycle testing for 500 h, the $(Y/Yb)_2SiO_5$ peaks decreased in intensity, and the α-cristobalite SiO_2 phase appeared, as shown in Figure 4b. SiO_2 presence after exposure may result from $Si(OH)_4(g)$ overpressure forming on the EBC's outer surface from SiC furnace tube oxidation, or from a signal artifact due to X-rays sampling near the edge of the coupon that's un-coated where regions of exposed SiO_2 scales are present.

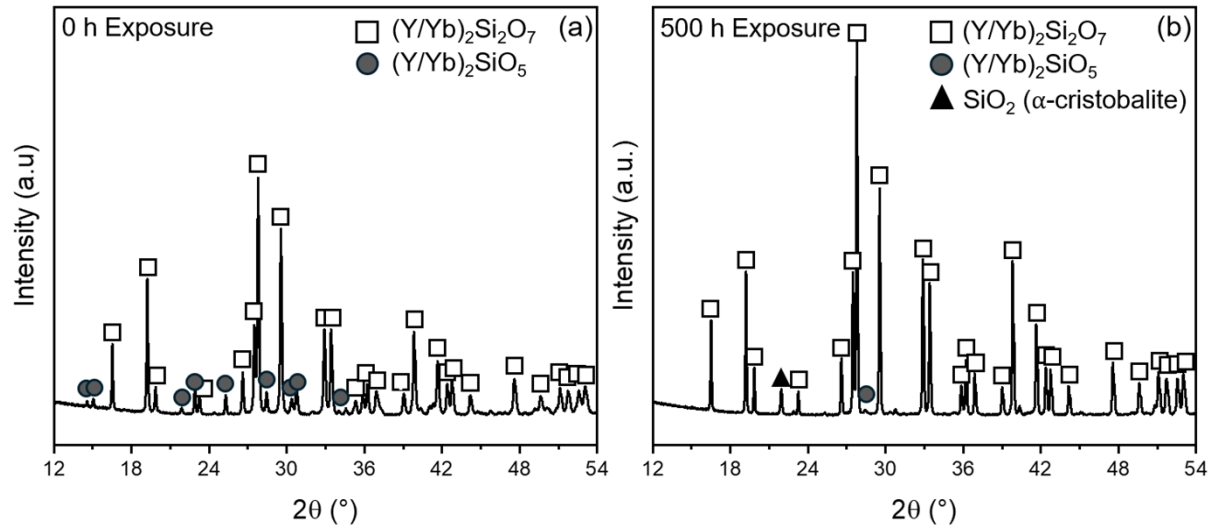

Figure 4: X-ray diffraction of $(Y/Yb)_2Si_2O_7$/Si coated Hexoloy for baseline (0 h) and after 1350°C, 90% H_2O + 10% O_2(g) cyclic exposure for 500 h.

3.4 TGO growth analysis after exposure

To accurately determine each specimen's oxidation state, a power law relationship [41], shown in Equation 3, was plotted alongside the TGO thickness measurements made via SOFIA.

$$x = K(t)^n \#(3)$$

where x = TGO thickness, K = oxidation rate constant, t = exposure time, and n = power law oxidation mechanism exponent.

Instead of using a linear or parabolic relationship, a double log plot of the TGO measurements and exposure time, shown in Figure 5a, was employed to determine the parameters of Equation 3. A linear slope was plotted for each SiC substrate's measurements where the slope of the line equals to n. By using the slope values calculated from the linear fits of the double log plots to get each datasets oxidation mechanism exponent n, TGO thickness (μm) vs. time $(h)^n$ was plotted where the slopes for each of the linear fits was calculated to get the K ($\mu m/t^n$) values. Utilizing both the found K and n values, a simulated power law curve fit was plotted for each

dataset's measured mean TGO thickness values. The fit vs. actual data for each sample exposures up to 500 h is presented in Figure 5b. Figure 5c provides a detailed view of the thickness measurements for the coated SiC specimens at the 500 h exposure time, highlighting the difference in TGO growth for each specimen.

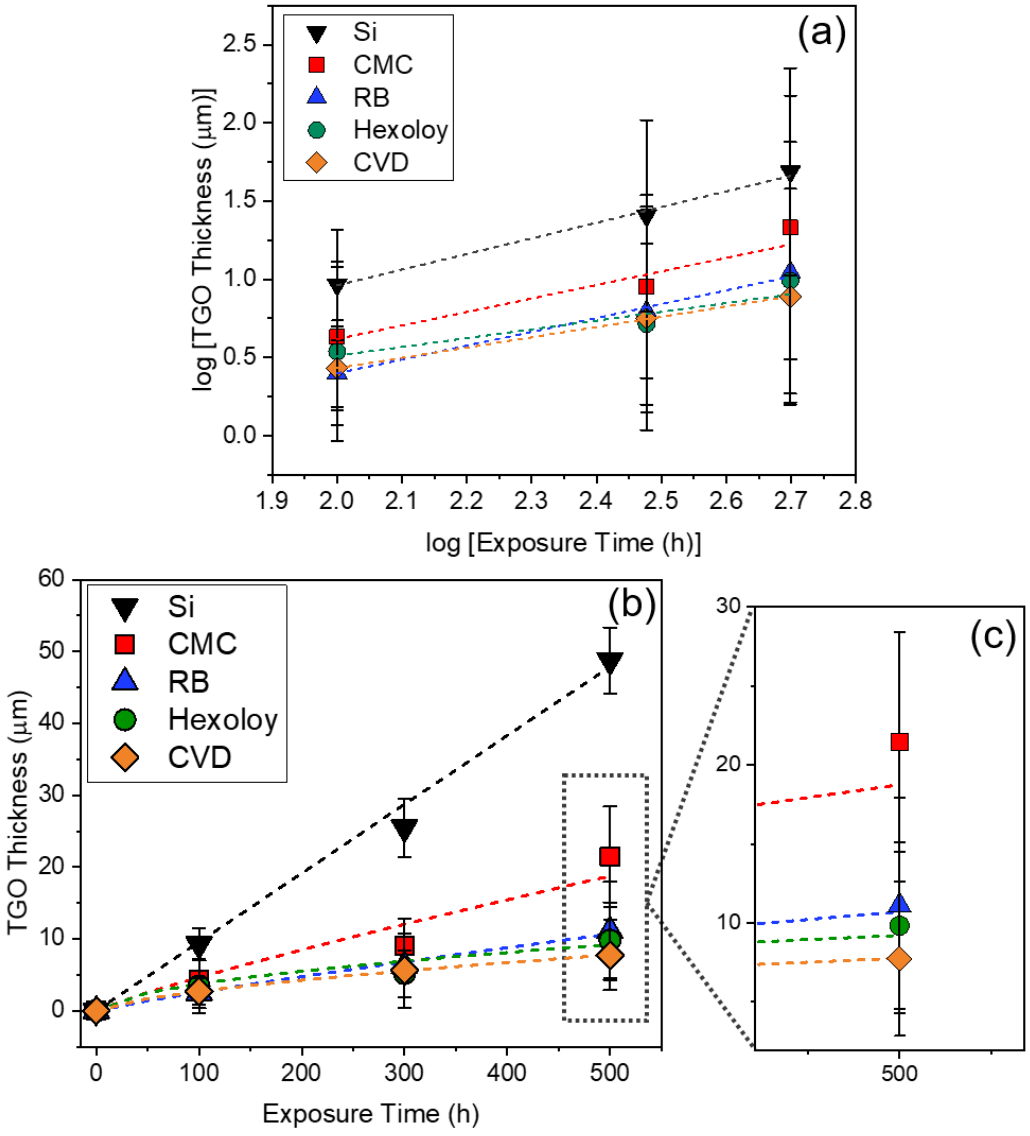

Figure 5: (a) Double log plot of the mean TGO thickness (µm) vs. time (h) after 1350ºC exposure to 90% H_2O + 10% O_2(g). (b) Mean TGO thickness of uncoated silicon, and $(Y/Yb)_2Si_2O_7$/Si-coated CMC, RB, Hexoloy, and CVD samples. (c) Zoomed in region of the coated SiC specimens after 500 h exposure. The error bars indicate the ± standard deviations.

TGO thickness measurements (counts) are presented in Table 4, while Table 5 provides the calculated *n* and *K* values for each dataset. Table 5 also includes the *K* values computed based on the classical linear relationship where $n = 1$ and the parabolic relationship where $n = 0.5$ depicted as $n_{classical}$ [42], facilitating a comprehensive comparison of growth rates among the specimens' TGOs.

Table 4: Mean ± standard deviation, median thickness of measured TGOs, and number of measurements (counts) for both bare Si and $(Y/Yb)_2Si_2O_7$ coated SiC specimens after 1350ºC exposure to 90% H_2O + 10% O_2(g) for 100 h, 300 h, and 500 h.

Specimen	Measurement	100 h	300 h	500 h
Bare-Si	mean (µm)	9.2 ± 2.2	25.5 ± 4.1	48.8 ± 4.6
	median (µm)	9.1	26.5	50.0
	counts	150	150	150
CMC	mean (µm)	4.3 ± 2.8	9.0 ± 3.8	21.4 ± 7.0
	median (µm)	3.7	8.5	21.4
	counts	9,847	8,994	9,759
RB	mean (µm)	2.5 ± 2.2	6.3 ± 4.4	11.1 ± 6.8
	median (µm)	1.8	5.0	9.6
	counts	10,104	10,572	9,983
Hexoloy	mean (µm)	3.4 ± 3.7	5.2 ± 3.3	9.8 ± 5.3
	median (µm)	2.4	4.4	8.4
	counts	10,092	10,045	9,978
CVD	mean (µm)	2.7 ± 1.9	5.6 ± 5.2	7.7 ± 4.9
	median (µm)	2.2	4.2	6.4
	counts	9,999	10,121	10,161

Table 5: Oxidation exponent (n) and oxidation rate constant (K) values from the power law fit for the TGO scales from the bare Si and $(Y/Yb)_2Si_2O_7$/Si-coated CMC, RB, Hexoloy, and CVD samples after 1350ºC exposure to 90% H_2O + 10% O_2(g) for 100 h, 300 h, and 500 h. Additional values for K are shown in terms of n = 1 for the classical linear growth rate and n = 0.5 for the classical parabolic growth rate.

Substrate	n	K (µm/t^n)	$n_{classical}$	K (µm/t^n)

Bare Si	1.00	0.10	1.00	0.09
Coated CMC	0.87	0.09	1.00	0.04
Coated RB	0.89	0.04	1.00	0.02
Coated Hexoloy	0.56	0.28	0.50	0.35
Coated CVD	0.66	0.13	0.50	0.30

Examining the TGO scale thicknesses, shown in Figure 5b, reveals that the coated CMC specimens have a faster growth rate than the other monolithic samples. At the 500 h exposure, the TGO thickness of the CMC samples (x = 21.45 μm) is twice that of the CVD, Hexoloy, and RB samples (x = 7.74, 9.83, 11.11 μm). The TGO growth is the highest for the uncoated silicon specimens (x = 48.77 μm), which is more than twice the thickness of the TGO on the CMC specimens.

The calculated oxidation exponent values for the monolithic SiC specimens show the coated Hexoloy and CVD specimens to have near-parabolic growth kinetics (n = 0.56, 0.66), and the RB and CMC datasets show near-linear growth kinetics (n = 0.89, 0.87). The RB TGO thickness values are similar to the TGO growth of the other coated monolithic SiC specimens. However, as shown in Figure 5c, the 500 h exposure exhibits growth delineation, with the TGO growth for the RB specimen's silicon bond coat increasing at a higher rate. The observed increase in TGO growth at the 500 h exposure may be attributed to a potential artifact related to the near-EBC failure, which could allow oxygen diffusion through the sides of the coated RB coupon [43]. Figure 6 highlights oxygen ingress near the edges of each tested coupon. SEM images of the CVD, Hexoloy, and RB coated specimens (Figure 6a-c) show similar edge oxidation with direct oxidation of the bond coat. However, to confirm if the RB specimens are close to failure, testing for more than 500 h is required. The CMC specimen (Figure 6d) exhibits significant fiber attack

at the exposed corners, which were grit blasted for coating preparation, removing its CVD seal coat. Below this area, the seal coat is present, resulting in less direct fiber attack.

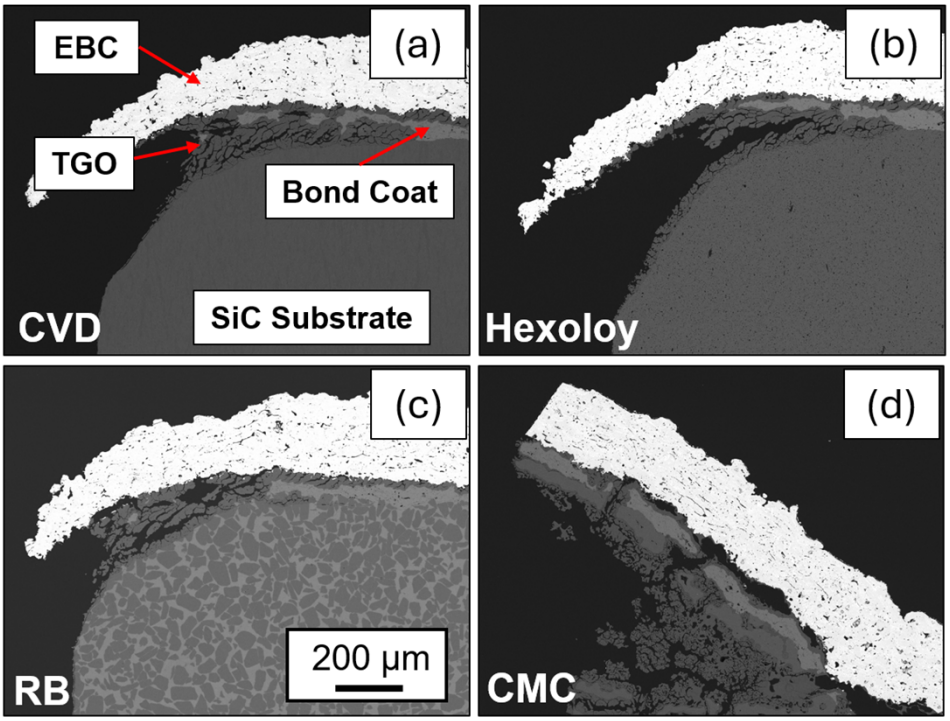

Figure 6: SEM images of the $(Y/Yb)_2Si_2O_7$/Si-coated (a) CVD, (b) Hexoloy, (c) RB, and (d) CMC samples after 500 h exposure to 90% H_2O + 10% O_2(g).

Comparison of the classical growth rate values (n = 0.5) for K for specimens following parabolic kinetics reveals that the coated Hexoloy samples exhibited an oxidation rate approximately 17% higher than the coated CVD samples ($K_{Hexoloy}$ = 0.35 µm/h^n; K_{CVD} = 0.3 µm/h^n). For specimens following linear oxidation kinetics (n = 1), the coated CMC specimens had a rate roughly twice that of the coated RB samples (K_{CMC} = 0.04 µm/h^n; K_{RB} = 0.02 µm/h^n).

The bare silicon specimens with linear SiO_2 scale growth had the highest growth kinetics for the linear kinetics specimens at K = 0.095 µm/h^n, which is expected because no EBC layer was present to act as a diffusion barrier. Additionally, limited SiO_2 volatilization, due to $Si(OH)_4$(g)

overpressure from the SiC reaction tube, may have contributed to the accelerated rate because the lack of volatilized species prevented linear–parabolic growth.

3.5 Deal and Grove analysis for TGO growth from silicon bond coats in EBC systems

Growth kinetics for the TGOs of the uncoated bare silicon, shown in Figure 7, were computed via the Deal and Grove model relationship [44]. The general relationship, shown in Equation 4, was utilized to plot against the measured TGO thickness after exposure.

$$x_{\text{oxide}}^2 + Ax_{\text{oxide}} = B(t + \tau)\#(4)$$

where A is related to the linear rate constant, B is the parabolic rate constant, x_{oxide} is the oxide scale thickness, t is time, and τ is the time correction to account for native oxide before oxidation exposure. This correction factor is given by Equation 5, where x_{oxide_0} represents the initial oxide present at $t = 0$.

$$\tau = \frac{x_{\text{oxide}_0}^2 + Ax_{\text{oxide}_0}}{B}\#(5)$$

Additionally, the uncoated silicon from this work was compared to extrapolated values at 1350°C for uncoated silicon in wet oxygen, reported by Deal and Grove [44] and shown in Figure 7.

A modified Deal and Grove model [45] accounts for the use of an EBC, shown in Figure 7b. The relationship is analogous to the traditional Deal and Grove model but uses a modified constant A to account for the thickness of the EBC layer, resulting in a new constant A'. In this context, the modification pertains to a single EBC layer, as represented by Equation 6

$$A' = A + \frac{2\gamma_{\text{oxide}}}{\gamma_{\text{coating}}}\delta\#(6)$$

where γ_{oxide} and $\gamma_{coating}$ represent the permeability of the oxidant species through the oxide scale and the coating layer, respectively, and δ denotes thickness of the coating layer. Furthermore, these

additional EBC layer terms result in the modified Deal and Grove relationship outlined in Equation 7.

$$x_{oxide}^2 + A' x_{oxide} = B(t + \tau) \quad (7)$$

A least squares regression analysis was performed to obtain the best fit for the measured x_{oxide} values by utilizing Equation 7 to solve for predicted x_{oxide} values. With this fit, the values for A', A, B, τ, and B/A were obtained from the experimental datasets shown in Figure 7b. These values are listed in Table 6. Initial TGO thicknesses x_{oxide_0} were assumed to be 0 μm at $t = 0$ in wet oxidation, as according to Deal and Grove [44].

Figure 7b shows a reference TGO dataset from K. Lee et al. [46] plotted alongside the other coated SiC substrates from this work. K. Lee's dataset consists of a modified $Yb_2Si_2O_7$ EBC/silicon bond coat system on a boron-containing SiC/SiC CMC exposed to 1350°C in 90% H_2O + 10% O_2(g). A larger TGO growth is observed for the coated CMC specimens in this work compared with the referenced TGO growth rates. The discrepancy may be due to different topcoat chemistries or different EBC layer thicknesses in the referenced dataset (EBC = 254 μm, silicon bond coat = 127 μm).

For the uncoated silicon specimen and its reference, shown in Table 6, a large discrepancy is observed in terms of the A and B constants and TGO thicknesses. The silicon TGO thickness measured in this research grows at a faster rate than the reference dataset from Deal and Grove. The variation in growth rates between the experimental results and the referenced results, also shown in Figure 7a, may be attributed to differences in the oxidation kinetics of silicon for this experimental research compared to those in the referenced procedure. The effect of high concentrations of $Si(OH)_4$(g) in the reaction tube during exposure could influence the TGO growth

rates, or the subsequent TGO cracking could lead to faster oxygen diffusion rates to the bare silicon due to thermal cycling.

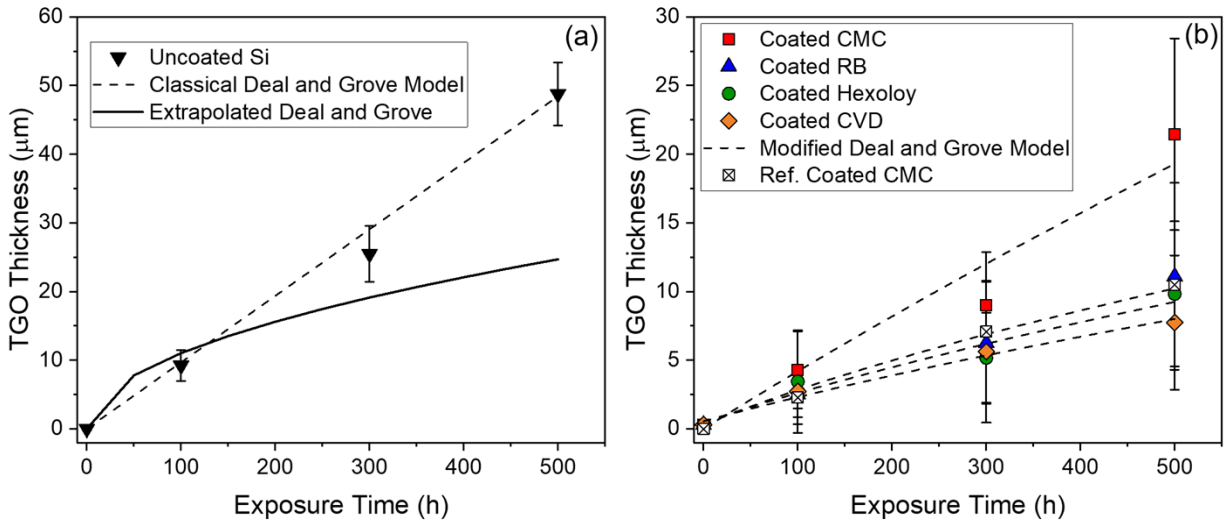

Figure 7: Deal and Grove analysis of mean TGO thickness measurements at 100 h, 300 h, and 500 h exposures to 1350°C in 90% H_2O + 10% O_2(g). (a) Uncoated silicon alongside a referenced silicon oxidation curve extrapolated from Deal and Grove [44] to 1350ºC in steam conditions [44]. (b) $(Y/Yb)_2Si_2O_7$/Si-coated CMC, RB, Hexoloy, and CVD after 1350ºC exposure to 90% H_2O + 10% O_2(g) with referenced TGO dataset from coated SiC/SiC-CMCs exposed to 1350ºC in 90% H_2O + 10% O_2(g) from K. Lee et al. [46]. The classic Deal and Grove model was fitted to the bare silicon specimen, and the modified Deal and Grove model was fitted to the coated specimens.

Table 6: Deal and Grove model analysis for 1350ºC, 90% H_2O + 10% O_2(g) exposed specimens.

Deal and Grove Model	**Substrate**	***A′* (µm)**	***A* (µm)**	***B* (µm²/h)**	***τ* (h)**	***B/A* (µm/h)**
Modified Deal and Grove (coated)	CVD	22.3	-	0.46	28	0.02
	Hexoloy	21	-	0.54	20	0.026
	RB	17.7	-	0.56	10	0.032
	CMC	145	-	6	0.001	0.044
Classic Deal and Grove	Si (this work)	-	2.62×10^{9}	2.54×10^{8}	0.0001	0.097
	Si (Deal and Grove)	-	0.021	1.22	0	58.10

The values determined using the Deal and Grove model were used to calculate the wet oxygen permeability of the TGO layers for the coated SiC specimens by employing the relationship in Equations 8 and 9 described by R. Sullivan [45].

$$\gamma_{oxide} = \frac{BN_1}{2P} \tag{8}$$

$$\frac{\gamma_{oxide}}{\gamma_{coating}} = \frac{A' - A}{2\delta} \tag{9}$$

Where N_1 = 4.5×10^{22} molecules/cm^3 for oxidation in H_2O [47], P = 1 atm, and δ are the EBC thickness values utilized from the mean EBC layer measurements reported in Table 3. When using values from Table 6, note that the A value, calculated from the uncoated silicon in this work, is higher than those extrapolated from Deal and Grove. This difference arises because Deal and Grove's data comes from isothermal testing, while this study uses thermally cycled testing. Uncoated thermally cycled oxide scales tend to crack and spall, causing a larger TGO scale and limiting the model's applicability for Equation 9 due to the large A value. In contrast, oxide scales grown on bond coats protected by EBC layers do not exhibit the same oxidation behavior in thermal cycle environments as uncoated oxide scales. Therefore, Deal and Grove's extrapolated A value was used for calculations using Equation 9. Additionally, the values for $\gamma_{coating}$ were determined by substituting Equation 8 into Equation 9 with Table 7 presenting the calculated permeability values, along with the ratio between the oxide and the coating $\frac{\gamma_{oxide}}{\gamma_{coating}}$.

As shown in Table 7, the wet oxygen permeability values for the EBCs are nearly the same for all of the coated monolithic and CMC specimens ($\gamma_{coating}$ equaling 9.10 × 10^{-12} to 1.63 × 10^{-11} mol·atm^{-1}·cm^{-1}·s^{-1}); the values for the CMC samples are only slightly higher, possibly due to slight differences with the EBC layer.

The wet oxygen permeability for the silicon bond coat TGOs of the coated monolithic specimens is different from that of the coated CMC specimen. The γ_{oxide} value for the TGO from

the coated CMC is approximately 12 times larger than that of the rest of the TGOs. The higher permeability aligns with the thicker TGO observed for the coated CMC samples after the high temperature exposure, likely to explain this discrepancy. Furthermore, the observed permeability values also align well with the values that have been reported for EBC systems coated onto SiC substrates.

A wet oxygen permeability of 1.23×10^{-12} mol·atm^{-1}·cm^{-1}·s^{-1} was predicted for a modeled $Yb_2Si_2O_7$ EBC in simulated 90% H_2O + 10% O_2(g) at 1316°C exposure by S. Singh et al. [48]. Additionally, a modeled silicon bond coat TGO wet oxygen permeability was estimated by S. Singh to be 3.74×10^{-14} mol·atm^{-1}·cm^{-1}·s^{-1} after simulated exposure to 90% H_2O + 10% O_2(g) at 1316°C. Moreover, R. Sullivan [45] estimated a $Yb_2Si_2O_7$ coating oxygen permeability at 3.73×10^{-13} mol·atm^{-1}·cm^{-1}·s^{-1} and the oxygen permeability through SiO_2 TGO to be 5.56×10^{-15} mol·atm^{-1}·cm^{-1}·s^{-1} at 1316°C in dry O_2(g).

The permeability ratios for all three coated monolithic SiC specimens are relatively consistent (0.052–0.042). Minor variations in permeability values are likely due to slight differences in EBC defect structure for each specimen. Conversely, the permeability ratio for the CMC specimens is different because of its TGO wet oxygen permeability value being approximately nine times greater than those of the other monolithic specimens.

Table 7: Wet oxygen permeability values for the coated SiC specimens after 1350ºC exposure to 90% H_2O + 10% O_2(g) for the permeability ratio and singular permeability values for the silicon bond coat TGO and the $(Y/Yb)_2Si_2O_7$ layer.

Substrate	$\gamma_{coating}$ (mole/atm·cm·s)	γ_{oxide} (mole/atm·cm·s)	$\frac{\gamma_{oxide}}{\gamma_{coating}}$
CVD	9.10×10^{-12}	4.77×10^{-13}	0.052
Hexoloy	1.05×10^{-11}	5.58×10^{-13}	0.053
RB	1.35×10^{-11}	5.71×10^{-13}	0.042

CMC	1.63×10^{-11}	6.23×10^{-12}	0.382

3.6 TGO defect analysis

SEM-BSE analysis was conducted on each specimen after cyclic exposures to 1350°C, 90% H_2O + 10% O_2(g) for 100 h, 300 h, and 500 h, shown in Figure 8. The TGO interface of each specimen is displayed to show the TGO scale growth evolution on the varying coated SiC substrates with respect to cyclic exposure time. Vertical through-cracks were visible for each of the SiO_2 scales from the silicon bond coats on the CVD, Hexoloy, and RB substrates, while through-cracks were rarely observed with the TGOs from the coated CMC substrates. Additionally, the coated Hexoloy specimens showed porosity within the TGO after 300 h and 500 h exposures (Figure 8f and j) that was not present for the other specimens.

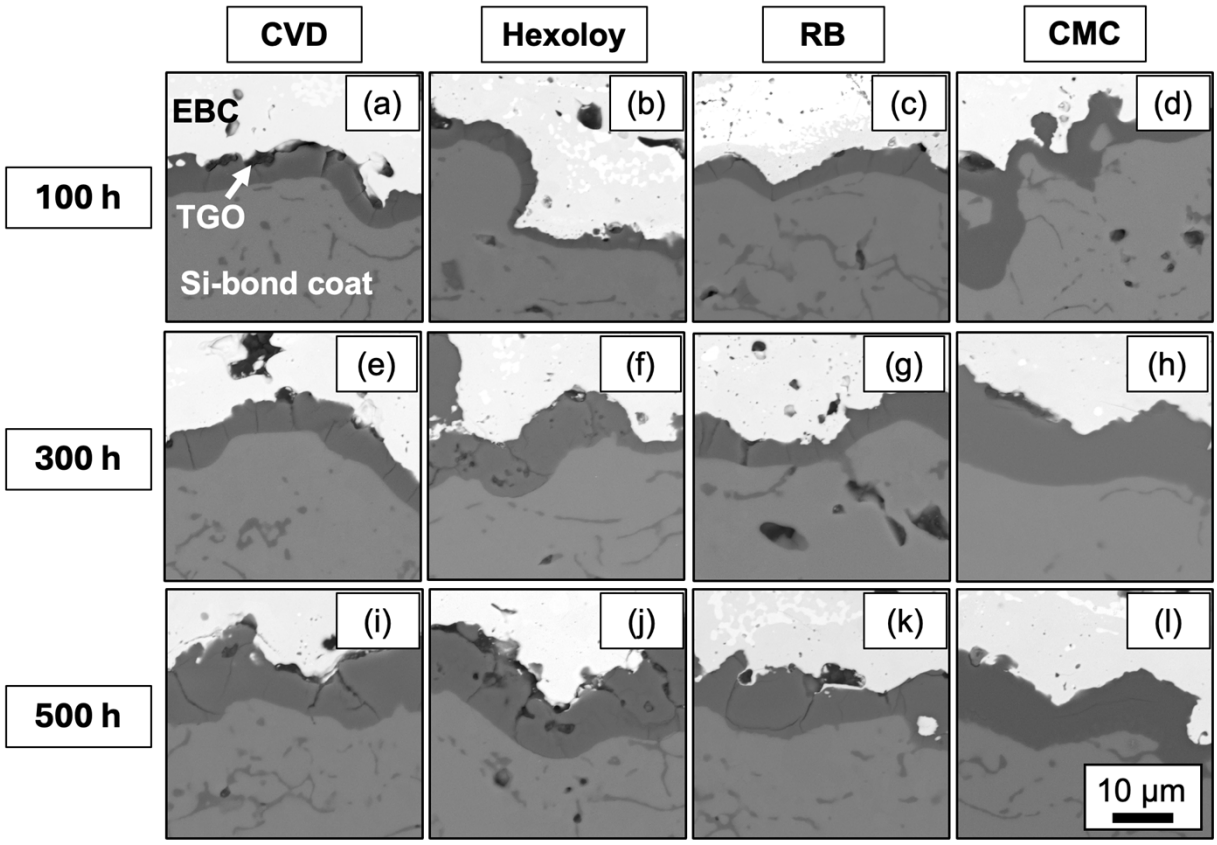

Figure 8: SEM-BSE analysis for $(Y/Yb)_2Si_2O_7$/Si coated SiC specimens after 1350ºC exposure to 90% H_2O + 10% O_2(g) for varying exposure times. SEM analysis of 100 h exposures shown for (a) CVD, (b) Hexoloy, (c) RB, and (d) CMC. SEM analysis of 300 h exposures shown for (e) CVD, (f) Hexoloy, (g) RB, and (h) CMC. SEM analysis of 500 h exposures shown for (i) CVD, (j) Hexoloy, (k) RB, and (l) CMC. The scale bar shown in (l) applies to all images shown.

The mean porosity and their respective standard deviations vs. exposure time are plotted in Figure 9a, which shows the TGO for the Hexoloy exposed samples to have the highest porosity and that the porosity increases with exposure time. The other coated SiC specimens do not show the same magnitude of porosity. Furthermore, the porosity for the CVD, RB, and CMC specimens are not much different in terms of standard deviation, with values less than 1%, as shown in Figure 9b. By contrast, Hexoloy exhibited approximately 2% and 3% porosity after 300 h and 500 h exposures, respectively.

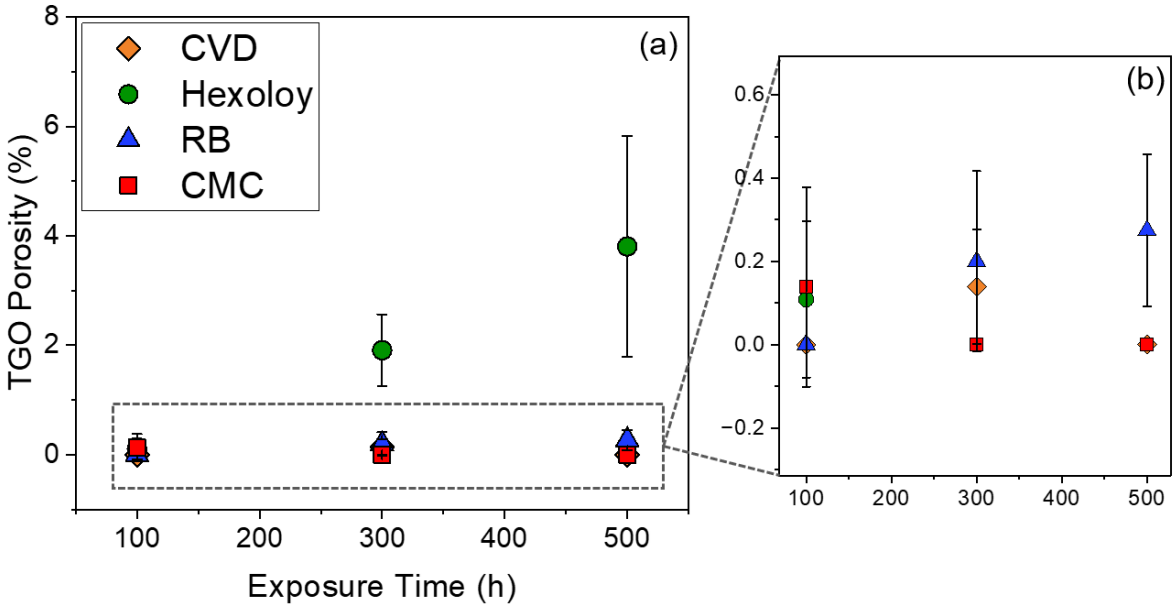

Figure 9: (a) TGO porosity for $(Y/Yb)_2Si_2O_7$/Si coated SiC substrates after exposure to 1350ºC in 90% H_2O + 10% O_2(g) for 100 h, 300 h, and 500 h. (b) Zoomed in region for the CVD, RB, and CMC's TGO porosity measurements. ImageJ qualitative analysis was used to measure porosity (%) for TGO's via SEM-BSE micrographs.

In Figure 8, the SEM micrographs show significant through-cracks in the TGO scale on the coated monolithic SiC specimens but little evidence of through-cracks for the coated CMC samples. TGO crack density and average crack spacing were calculated, with the TGO crack density visualized in Figure 10a and shown in Table 8. The coated monolithic SiC specimens have a similar TGO crack density; only Hexoloy TGO crack density is slightly higher at the lower exposure times. However, the coated CMC specimens have a significantly lower crack density overall at each exposure time, and the crack density at the 500 h exposure is about one-seventh that of the rest of the coated SiC samples.

Additionally, average crack spacing values, graphed in Figure 10b, exhibit similar spacing growth in terms of exposure time for the SiO_2 scales from the $(Y/Yb)_2Si_2O_7$/Si-coated monolithic SiC specimens, but a larger through-crack spacing was measured for the coated CMC samples due to minimal crack distribution along the TGO scales.

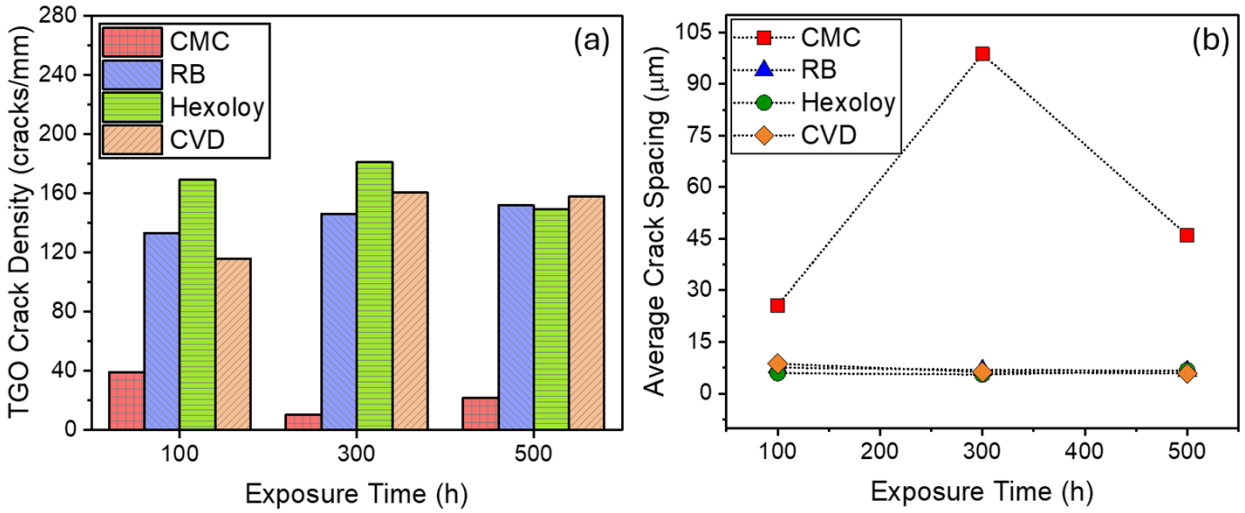

Figure 10: Through-crack analysis performed on TGOs for each $(Y/Yb)_2Si_2O_7$/Si-coated SiC substrate after exposures at 1350°C in 90% H_2O + 10% O_2(g) for 100 h, 300 h, and 500 h. Two graphs show (a) plotted data for the TGO through crack density for each specimen and (b) the mean through-crack spacing within each specimen TGO.

Table 8: ImageJ measurements of TGO through-cracks from $(Y/Yb)_2Si_2O_7$/Si-coated SiC substrates after exposures at 1350°C in 90% H_2O + 10% O_2(g) for 100 h, 300 h, and 500 h. Through-crack measurements were taken from four micrographs; distance measured was 0.691 mm for each sample.

Specimen	Time (h)	No. of cracks	cracks/mm
CVD	100	80	115.77
	300	111	160.64
	500	109	157.74
Hexoloy	100	117	169.32
	300	125	180.90
	500	103	149.06
RB	100	92	133.14
	300	101	146.16
	500	105	151.95
CMC	100	27	39.074
	300	7	10.13
	500	15	21.71

The observed microstructural results indicate slight differences in the TGO for the monolithic SiC specimens, with the coated Hexoloy TGO scales exhibiting the highest TGO through-crack density at 100 h and 300 h, and a higher porosity percentage than the other coated SiC samples. Furthermore, the coated CMC samples show the most significant overall difference, with minimal defect microstructures observed in terms of porosity and crack density. Because of the structural differences between the coated CMC TGOs and those of the other samples, the SiO_2 scales are suspected to be compositionally and structurally distinct from the other coated monolithic SiC comparisons.

3.7 Phase and chemical analysis of TGO scales post-exposure

To investigate the TGO phases, Raman spectroscopy analysis was performed on all $(Y/Yb)_2Si_2O_7$/Si-coated SiC specimens after 1350ºC exposure in 90% H_2O + 10% O_2(g) for 500 h. The plotted Raman spectra, shown in Figure 11a, indicate that the TGO for the CMC samples lack the cristobalite α-SiO_2 peaks at approximately 115, 230, and 415 cm^{-1} [49], but these peaks are present in the coated monolithic samples, with the addition of small α-SiO_2 peaks observed for the Hexoloy specimen at 786 cm^{-1} and 1078 cm^{-1}. Figure 11b displays a zoomed-in Raman spectrum for each specimen, showing more detail of the Raman peaks for the α-SiO_2 phase. The primary peak for silicon, seen in each spectrum, comes from the silicon bond coat. The primary silicon peak is slightly shifted to the left at 519 cm^{-1} from its predicted position at ~521 cm^{-1} [50] for the CMC sample, suggesting possible chemical bond lengthening and tensile stresses present. Additionally, the silicon peaks at 620 cm^{-1} and 948 cm^{-1} [50], [51] are observed on the CMC sample.

The absence of α-SiO_2 peaks in the CMC specimens indicates the presence of an amorphous TGO. By contrast, the other coated SiC specimens (i.e., CVD, Hexoloy, and RB) exhibit the anticipated cristobalite peaks at approximately 115, 230, and 415 cm^{-1} confirming their crystalline nature.

Furthermore, boron species have been shown to diffuse toward the TGO [34], and boron has been shown to disrupt SiO_2 network properties [52], which is suspected to be causing the difference in TGO properties for the CMC and Hexoloy specimens. However, any expected borosilicate bonds are not present at around 470 cm^{-1} for the Hexoloy and CMC specimens, and no B_2O_3 boroxol ring peaks are seen at around 800 and 808 cm^{-1} [53]. Therefore, the data suggests that very low concentrations must be present within the TGOs of the CMC and Hexoloy specimens after 500 h, suggesting high volatility of boron species at the TGO interface at these temperatures.

The Raman spectroscopy analysis confirms the presence of an amorphous structure in the TGO of the CMC specimen after 500 h of exposure, in contrast to the crystalline TGO observed in the other SiC substrate specimens. Additionally, this amorphous structure is likely also present in the coated CMC specimens exposed for 300 h and 100 h, as indicated by their low crack density values. Therefore, network modification of the TGO in the $(Y/Yb)_2Si_2O_7$/Si-coated CMC specimens from boron species are likely occurring, while network modification is most likely not occurring for the coated Hexoloy specimens that exhibited crystalline TGO scales.

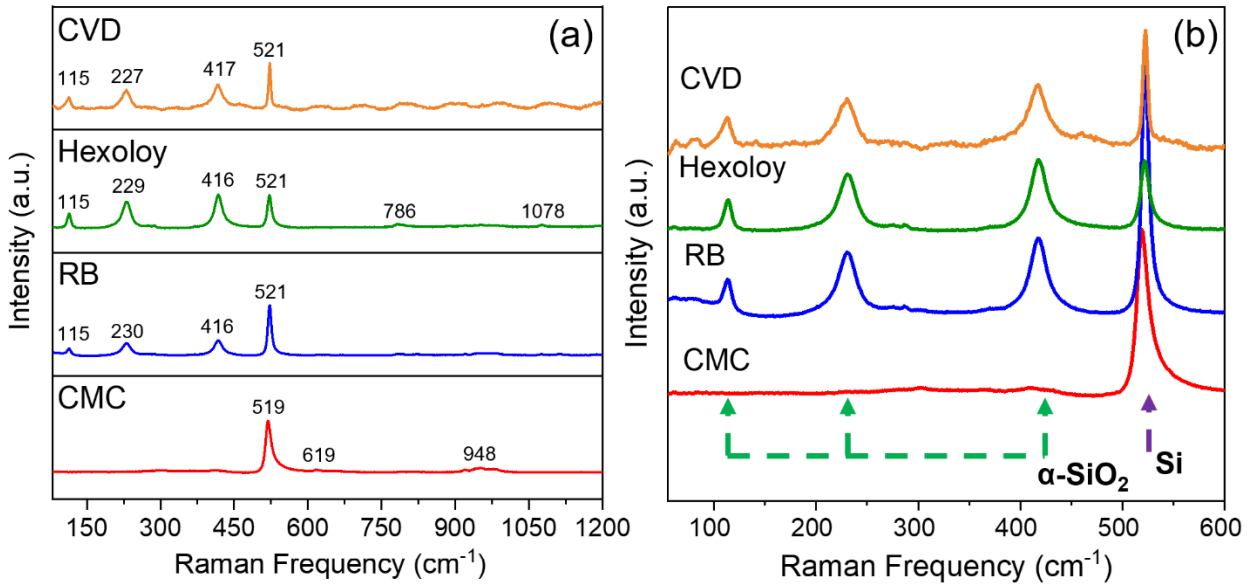

Figure 11: (a) *Raman spectroscopy analysis of TGO scales from* $(Y/Yb)_2O_2O_7$*/Si-coated SiC specimens (CVD, Hexoloy, RB, CMC) after 500 h exposure to 1350ºC in 90%* H_2O *+ 10%* O_2*(g). (b) High magnification area of the spectra showing cristobalite α-*SiO_2 *peaks shown for ~113, 230, and 415* cm^{-1} *and Si peak shown for ~521* cm^{-1} *for all four samples after exposure. Noise in the CVD spectra is due to the artifact of background fluorescence that occurred during its sampling.*

To investigate coated substrates further, EPMA map analysis was conducted on all four $(Y/Yb)_2Si_2O_7$/Si-coated SiC substrates after 500 h exposure. The top left row of Figure 12, shows the SEM-BSE images for each substrate (Figure 12a-d) on top of the signals for oxygen, silicon, carbon, and yttrium (yttrium representative of the rare-earth signal in the EBC layer). For all four specimens, the TGO primarily shows a signal for oxygen which is displayed in the second row on the left (Figure 12e-h) and silicon shown in the left third row (Figure 12i-l) for the SiO_2 scale. Additionally, the carbon signal shown in the bottom-left row (Figure 12q-t) is observed to be present within both the EBC layer and substrate for each specimen, but primarily this is attributed as an artifact of the epoxy within cracks and pores of the samples.

For the CMC and Hexoloy specimens (Figure 12u and v), prominent wt.% concentrations of boron are still present after the 500 h exposure, as shown in panels (w) and (x) in Figure 12.

However, the EPMA maps did not detect boron within the TGO for either CMC or Hexoloy specimen.

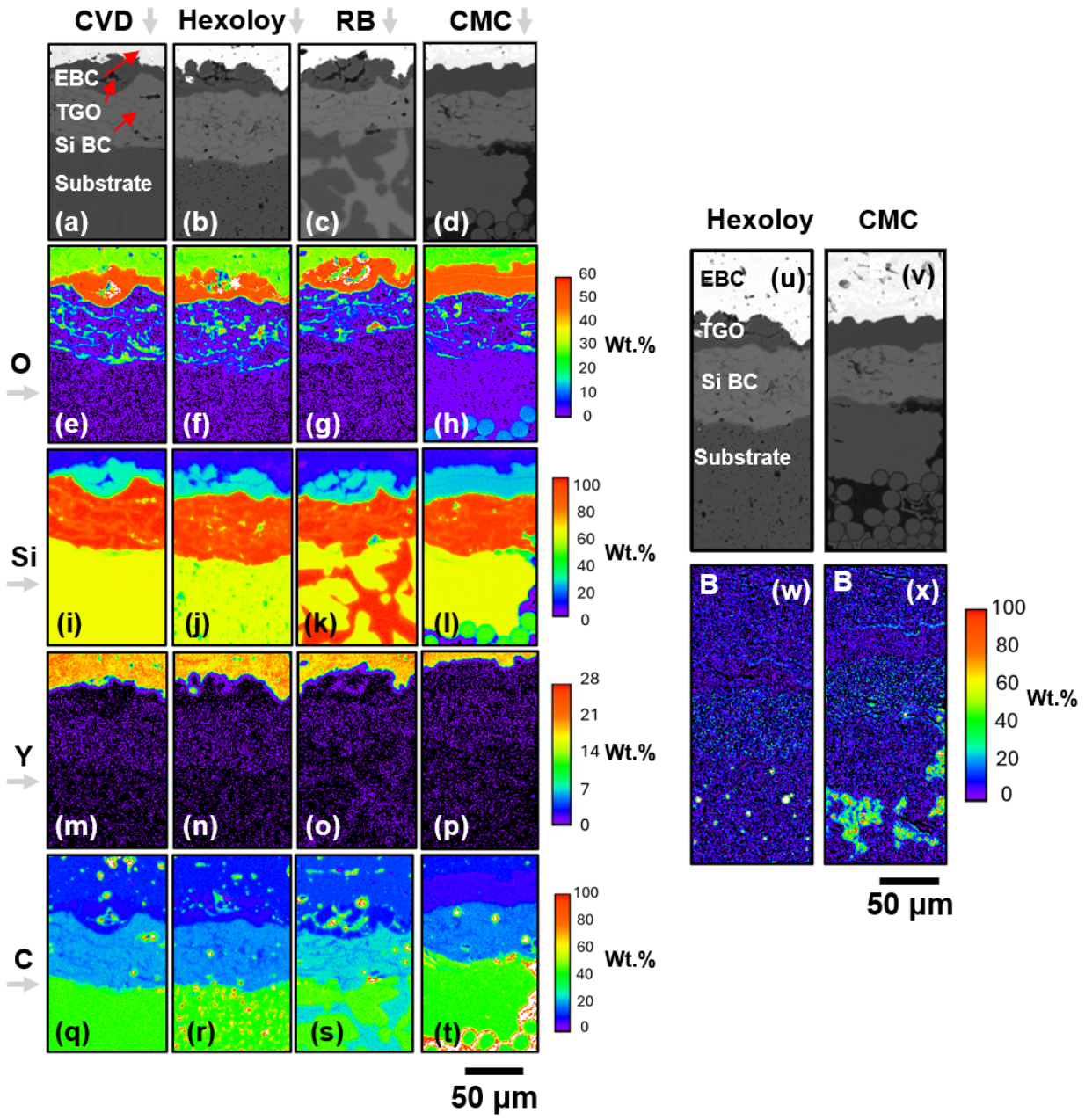

Figure 12: EPMA analysis of specimens after 500 h exposure to 1350°C in 90% H_2O + 10% O_2 (g). SEM-BSE imaging of coated (a) CVD, (b) Hexoloy, (c) RB, and (d) CMC specimens. EPMA elemental map analysis of for all four SiC substrates for (e-h) O, (i-l) Si, (m-p) Y, and (q-t) C in wt.%. The Hexoloy (u) and CMC sample (v) are shown alongside their B wt.% maps (w and x).

Chemical point analysis via EPMA (~ 18 measurements per sample) was performed on the TGO scales of the $(Y/Yb)_2Si_2O_7$/Si-coated CMC samples after 100 h, 300 h, and 500 h exposures to investigate the expected boron impurities in its TGO scales due to each specimen's low crack density and the observed amorphous TGO at the 500 h exposure.

Because of the irregularities with the CVD SiC seal coat over the CMC fiber tows, the applied silicon bond coat was either directly over the seal coat or the fiber tow. Additionally, the boron-containing phases where shown to be near the fiber tows, suggesting that a higher boron enrichment may be present in TGO scales grown near these regions. Therefore, point EPMA analysis was conducted on TGOs positioned either above the seal coat regions or above the fiber tow regions to see if there was a difference in boron content.

The results confirm boron to be present within the TGOs for the coated CMC specimens. Figure 13 shows SEM images of the CMC specimen after 100 h as an example of the TGO regions above the fiber tow (Figure 13a) and the seal coat (Figure 13b). Furthermore, the results showed that there was a higher boron content (wt.%) within the TGO above the fiber tows overall, with the mean wt.% for boron slightly increasing with exposure time, visually shown in Figure 13c. Additionally, the boron content in the TGO near the seal coat remains close to zero until the 500 h exposure mark, where an average value of 1.02 wt.% was recorded, visually shown in Figure 13c. Furthermore, the total mean boron content throughout the TGO scale for each sample showed a relatively low value of boron up until the 500 h exposure, shown in Figure 13d, with a mean total going from 0.56 to 1.25 wt.%.

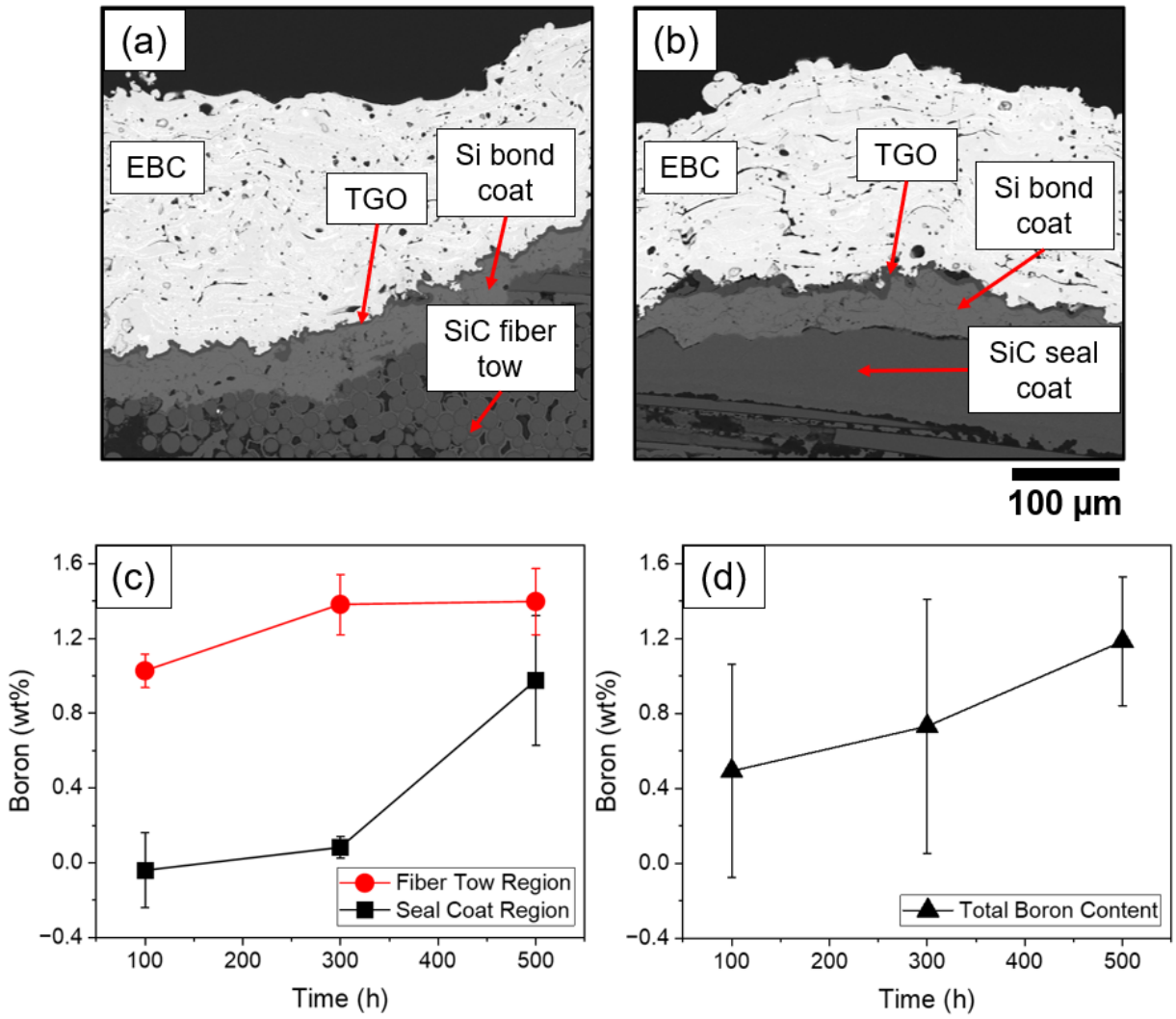

Figure 13: EMPA analysis for boron wt.% in the TGO phase for the coated CMC specimens exposed to 90% H_2O + 10% O_2 (g) at 1350°C for 100 h, 300 h, and 500 h. SEM-BSE images of CMC specimen after 100 h exposure for TGO regions above (a) the fiber tow region and (b) the seal coat region. (c) Graph of boron wt.% in the TGO above either the seal coat region or fiber tow region regarding exposure time. (d) Total mean boron wt.% detected within the TGO at each exposure time.

Further EMPA point analysis was done on the silicon bond coat layer for each of the exposed CMC specimens. However, results for the 100 h and 300 h exposures showed relatively negative results with only the 500 h exposure indicating small amounts of boron concentration with a mean value of 0.2 wt.%. The low concentration levels could be caused by the relatively

high defect structure of the bond coat leading to short circuit diffusion of the boron species through the layer.

4.0 Discussion

Systematic analysis of TGO properties from $(Y/Yb)_2Si_2O_7$/Si-coated CVD, Hexoloy, RB, and CMC were investigated after high-temperature cyclic exposure to 1350°C in 90% H_2O + 10% O_2(g) for 100 h, 300 h, and 500 h. The investigation primarily compares the monolithic SiC substitutes (i.e., CVD, Hexoloy, RB), commonly used for low-cost lab-scale testing, to the more applicable CMC to evaluate how the EBC system's TGO may be altered from substrate utilization. Results from the study show a clear difference in TGO properties between the monolithic SiC samples and the CMC specimens, with TGO crystallinity being the main factor that is affected.

4.1 Dopant effects on TGO growth

Analyzing the TGO thicknesses for each of the $(Y/Yb)_2Si_2O_7$/Si-coated SiC substrates after high-temperature exposure to the steam environment showed that the CMC specimens have the highest TGO growth rate. Additionally, wet oxygen permeability values calculated from the SiO_2 scales after exposure showed the amorphous TGO from the CMC specimens to be 12 times larger than the other crystalline TGOs. Furthermore, the wet oxygen permeability for all the EBC layers is shown to be higher than the silicon bond coat TGOs. This result confirms that for these samples the SiO_2 scale is the rate-controlling step for oxide growth of the silicon bond coat. Therefore, the formation of an amorphous SiO_2 scale from the silicon bond coat can be predicted to directly result in a thicker TGO scale.

The observation of thicker TGO growth for amorphous SiO_2 than crystalline SiO_2 has been reported by D. Scotson et. al. [54]. They describe how TGO density affects oxygen diffusivity, with faster diffusion rates observed for amorphous SiO_2 due to its relatively lower density (2.20 g/cm^3) than β-cristobalite (2.32 g/cm^3) [55]. Furthermore, dopants from B_2O_3 can increase oxygen diffusivity in SiO_2 at high temperatures by roughly five times compared with a crystalline SiO_2 network [55], [56]. Oxygen diffusivity increases because boron doping breaks down Si–O bonds and expands the SiO_2 network through vitrification. Additionally, the presence of boron in high-temperature oxidating environments can have detrimental effects on high-temperature stability. For example, B_2O_3 has a low melting temperature around 450°C and an even lower eutectic melt with SiO_2 around 372°C [57], [58].

Differences in TGO crystallinity can also affect stress states for the TGO and EBC layers, with reports showing amorphous forming SiO_2 having a higher internal compressive stress than crystalline TGOs. Amorphous SiO_2 has a larger coefficient of thermal expansion mismatch (0.6×10^{-6} K^{-1}) to silicon (4.1×10^{-6} K^{-1}) than β-cristobalite (3×10^{-6} K^{-1}) [20], [59], [60], leading to the accumulation of high thermomechanical stresses during thermal cycling at the bond coat–TGO interface. Furthermore, these elevated compressive and tensile stresses of an amorphous TGO scale can eventually cause significant stress of the bond coat layer beneath the TGO, leading to spallation of the coating [16]. In contrast, the stress states in crystalline SiO_2 scales relieve accumulated thermomechanical stresses through cracking of the TGO scale [17], which occurs during the phase transformation of cristobalite SiO_2 at about 230ºC during cooling [54].

4.2 Boron effects on TGO microstructure and phase

The amorphous structure of the TGO scales observed for the coated CMC specimens, as confirmed by Raman spectral analysis, along with the detection of boron in the TGO scales using EPMA point analysis, indicates that boron compounds have diffused from the CMC substrate through the silicon bond coat to the oxide scale. During the formation of the initial SiO_2 scale, its structure is assumed to be amorphous until it crystallizes to the β-cristobalite phase between 700°C and 1400°C; the crystallization temperature range is large due to SiO_2 doping sensitivity [61]. Because of this doping sensitivity, the crystallization temperature can be altered by binary boron-containing dopants that hinder devitrification by increasing activation energies needed for molecular ordering. Boron as a dopant acts as a glass modifier and will disrupt silica networks by creating B–O–Si bonds and decreasing tetrahedrally coordinated Si–O–Si bond density, which overall reduces the long-range order of the system. Consequently, activation energy for molecular rearrangement increases, enhancing the stability of the amorphous structure at temperatures exceeding the reported crystallization temperatures of the SiO_2 scale.

A proposed mechanism of this effect has been discussed by I. Crystal et. al. [62], who investigated preventing cristobalite formation of TGOs from SiC substrates. Within the work they incorporate 3.4 wt.% of B_4C dopants into the bulk, where the B_4C is theorized to oxidize (~780°C–850°C) to CO_2 and B_2O_3, and then the B_2O_3 will melt at around 450°C and eventually vaporize at around 1100°C, causing enough disruption to the SiO_2 scales to prevent crystallization, even up to 1500°C. The low weight percentage of boron doping aligns with the low concentrations observed in this study using EPMA analysis, which detected levels up to approximately 1.6 wt.% within the amorphous TGOs for the CMC specimens.

The EPMA maps of the baseline SiC substrates reported in this work show large boron compounds in the CMC substrate around the fiber tows but smaller, more sporadic boron

compounds in the Hexoloy substrate. This lower boron concentration in the Hexoloy specimens is possibly insufficient to diffuse and dope the SiO_2 scale to prevent β-cristobalite formation during the high-temperature exposures at 1350°C.

The presence of porosity in the Hexoloy TGO specimens could be from possible buildup of CO_2(g) and B_2O_3(g) species from boron/carbon compound oxidation from the substrate, as well as additional HBO_2/H_3BO_3(g) formation in the steam environment [63]. Additionally, at high temperatures B_2O_3 has a relatively large vaporization rate ($k_{vap} \approx 0.04$ (mg/cm^2)^2 min^{-1} at 1300°C, $P_{O2} = 3.3 \times 10^4$ Pa) [64] that can also cause some B_2O_3(g) formation in the TGO scale.

The relatively higher viscosity at 1350°C for the devitrified TGOs of the Hexoloy samples, might explain the lack of pore formation in the SiO_2 scale for the CMC specimens [65]. The amorphous glass network in the CMC TGOs is expected to exhibit a relatively lower viscosity level that can allow for defect healing due to viscous flow at the high-temperature exposures [66], which may explain the low porosity within its scales from gaseous boron species that were expected to form during high temperature exposures.

Additionally, the boron dopant levels for the amorphous CMC specimen at 500 h was recorded with variations of concentration throughout the TGO layer depending on if the sampled region was either above the CVD SiC seal coat or above the SiC fiber tows. The EPMA point analysis shows that the TGO has a higher concentration of boron when the silicon bond coat is directly above the fiber tows and not the CVD SiC seal coat. The variation of boron concentrations shows how the seal coat for the CMC specimens acts as a diffusion barrier for highly mobile species at high temperatures, most likely due to its highly dense structure. Further testing is needed in order to fully understand boron migration through SiC substrates at these high temperature conditions.

4.3 Considerations for lab-scale analysis

Because of the accelerated growth seen for amorphous TGOs produced from coated CMC substrates, the monolithic SiC substrates used in this study for EBC testing do not represent an accurate comparison. The CVD, Hexoloy, and RB specimens do not contain the concentrations of sintering additives and processing aids that act as SiO_2 network modifiers. The results of this work show that SiC substrate dopants can transport through the silicon bond coats and alter their TGO growth rates and crystallinity, most notable boron. Future research should carefully consider the sensitivity of TGO dopants and should aim to be capable of producing TGO scales comparable to those observed under turbine conditions.

When conducting lab-scale EBC testing, if assumed that the seal coat over the CMC substrate is perfect, the CVD monolithic SiC substrate will provide the most accurate TGO characteristics. However, if assumed the CMC seal coat is imperfect (due to thermal cycling damage or manufacturing defects), it would be necessary to use a monolithic SiC specimen with added boron-containing dopants to obtain a more accurate TGO morphology. Furthermore, future research should test EBC systems on SiC substrates with different concentrations of boron additives to systematically study their impact on TGO scale growth and structure.

5 Conclusion

The systematic research described herein demonstrates the effects that monolithic SiC and SiC/SiC CMC substrates have on EBC systems during high-temperature steam exposures at 1350°C in 90% H_2O + 10% O_2(g) for 100 h, 300 h, and 500 h. The following results were observed:

1. Boron species from the SiC substrate significantly influence the formation and characteristics of the silicon bond coat TGO scales during high-temperature steam exposure.
2. TGOs formed in the presence of boron in the SiC substrate can produce an amorphous SiO_2 scale due to SiO_2 structure doping caused by boron-containing species migrating from the substrate through the silicon bond coat.
3. An amorphous TGO can have more than 10× the wet oxygen permeability in comparison to crystalline cristobalite TGOs, increasing the oxidation rate of the silicon bond coat and allowing the TGO layer to grow at a faster rate.

Overall, the research emphasizes the variations in SiC chemistries and how they can influence EBC systems. Lab-scale research should consider how the structural differences between monolithic SiC and CMCs can alter EBC system performance. Such considerations will be essential for advancing the combustion turbine engine field and improving the performance and durability of EBC systems.

6 Acknowledgements

This project was funded by the U.S. Department of Energy (DOE), Office of Fossil Energy and Carbon Management, project FEAA300 under contract DE-AC05-00OR22725 with Oak Ridge National Laboratory (ORNL) managed by UT Battelle, LLC. Dr. Edgar Lara-Curzio from ORNL oversaw its management. Special thanks to Bryan Harder at NASA Glenn for providing CMC specimens; S. Sampath and E. Garcia-Granados from Stony Brook University for applying the EBC layer; Dr. Bruce Pint (retired, ORNL) for his advice and conceptual input; Jim Horenburg from ORNL's Metallography Division for mounting, cross-sectioning, and polishing the

specimens; George Garner and Michael Alexander for conducting cyclic furnace experiments; and Trevor G. Aguirre for his technical review at ORNL. Access to the Raman spectrometer was provided by the Nuclear Nonproliferation Division, Oak Ridge National Laboratory.

7 References

[1] K. P. L. Fullagar, R. W. Broomfield, M. Hulands, K. Harris, G. L. Erickson, and S. L. Sikkenga, "Aero Engine Test Experience With CMSX-4® Alloy Single-Crystal Turbine Blades," *J. Eng. Gas Turbines Power*, vol. 118, no. 2, pp. 380–388, Apr. 1996, doi: 10.1115/1.2816600.

[2] N. P. Padture, M. Gell, and E. H. Jordan, "Thermal Barrier Coatings for Gas-Turbine Engine Applications," *Science*, vol. 296, no. 5566, pp. 280–284, Apr. 2002, doi: 10.1126/science.1068609.

[3] D. Tejero-Martin, C. Bennett, and T. Hussain, "A review on environmental barrier coatings: History, current state of the art and future developments," *J. Eur. Ceram. Soc.*, vol. 41, no. 3, pp. 1747–1768, Mar. 2021, doi: 10.1016/j.jeurceramsoc.2020.10.057.

[4] K. N. Detwiler and E. J. Opila, "Oxidation of SiC/BN/SiC ceramic matrix composites in dry and wet oxygen at intermediate temperatures," *J. Eur. Ceram. Soc.*, vol. 42, no. 10, pp. 4110–4120, Aug. 2022, doi: 10.1016/j.jeurceramsoc.2022.04.003.

[5] J. A. DiCarlo, H.-M. Yun, G. N. Morscher, and R. T. Bhatt, "SiC/SiC Composites for 1200°C and Above," in *Handbook of Ceramic Composites*, N. P. Bansal, Ed., Boston, MA: Springer US, 2005, pp. 77–98. doi: 10.1007/0-387-23986-3_4.

[6] T. Nakamura, T. Oka, K. Imanari, K. Shinohara, and M. Ishizaki, "Development of CMC turbine parts for aero engines," *IHI Eng. Rev.*, vol. 47, no. 1, pp. 29–32, 2014.

[7] E. J. Opila, "Oxidation and Volatilization of Silica Formers in Water Vapor," *J. Am. Ceram. Soc.*, vol. 86, no. 8, pp. 1238–1248, Aug. 2003, doi: 10.1111/j.1151-2916.2003.tb03459.x.

[8] A. J. Fernández-Carrión, M. D. Alba, A. Escudero, and A. I. Becerro, "Solid solubility of Yb2Si2O7 in β-, γ- and δ-Y2Si2O7," *J. Solid State Chem.*, vol. 184, no. 7, pp. 1882–1889, Jul. 2011, doi: 10.1016/j.jssc.2011.05.034.

[9] J. Felsche, "The crystal chemistry of the rare-earth silicates," in *Rare Earths*, vol. 13, in Structure and Bonding, vol. 13. , Berlin, Heidelberg: Springer Berlin Heidelberg, 1973, pp. 99–197. doi: 10.1007/3-540-06125-8_3.

[10] K. N. Lee, D. S. Fox, and N. P. Bansal, "Rare earth silicate environmental barrier coatings for SiC/SiC composites and Si3N4 ceramics," *J. Eur. Ceram. Soc.*, vol. 25, no. 10, pp. 1705–1715, Jan. 2005, doi: 10.1016/j.jeurceramsoc.2004.12.013.

[11] K. M. Grant, S. Krämer, J. P. A. Löfvander, and C. G. Levi, "CMAS degradation of environmental barrier coatings," *ICMCTF 2007*, vol. 202, no. 4, pp. 653–657, Dec. 2007, doi: 10.1016/j.surfcoat.2007.06.045.

[12] L. C. Hoffman, B. J. Harder, and M. J. Presby, "Foreign Object Damage of an Environmental Barrier Coated Ceramic Matrix Composite," in *GT2025*, Volume 1: Aircraft Engine; Ceramics and Ceramic Composites, Jun. 2025. doi: 10.1115/GT2025-152547.

[13] E. Kawai *et al.*, “Crack Initiation Criteria in EBC under Thermal Stress,” *Coatings*, vol. 9, no. 11, p. 697, Oct. 2019, doi: 10.3390/coatings9110697.
[14] B. J. Harder, M. J. Presby, J. A. Salem, S. M. Arnold, and S. K. Mital, “Environmental Barrier Coating Oxidation and Adhesion Strength,” *J. Eng. Gas Turbines Power*, vol. 143, no. 031004, Feb. 2021, doi: 10.1115/1.4049414.
[15] J. Luo, W. Yang, L. Chen, and G. Yang, “Silicon-based bond coatings for environmental barrier coatings: Present status and prospective,” *Int. J. Appl. Ceram. Technol.*, vol. 21, no. 6, pp. 3771–3788, Nov. 2024, doi: 10.1111/ijac.14840.
[16] T. G. Aguirre, L. Lin, M. J. Ridley, K. A. Kane, and B. A. Pint, “Finite Element Modeling of the Phase Change in Thermally-Grown SiO2 in SiC Systems for Gas Turbines,” *JOM*, vol. 76, no. 8, pp. 4131–4145, Aug. 2024, doi: 10.1007/s11837-024-06507-4.
[17] M. J. Lance, M. J. Ridley, K. A. Kane, and B. A. Pint, “Raman spectroscopic characterization of SiO_2 phase transformation and Si substrate stress relevant to EBC performance,” *J. Am. Ceram. Soc.*, vol. 106, no. 10, pp. 6205–6210, Oct. 2023, doi: 10.1111/jace.19190.
[18] K. N. Lee, “Yb_2 Si_2 O_7 Environmental barrier coatings with reduced bond coat oxidation rates via chemical modifications for long life,” *J. Am. Ceram. Soc.*, vol. 102, no. 3, pp. 1507–1521, Mar. 2019, doi: 10.1111/jace.15978.
[19] A. J. Perrotta, D. K. Grubbs, E. S. Martin, N. R. Dando, H. A. McKinstry, and C. Huarg, “Chemical Stabilization of β-Cristobalite,” *J. Am. Ceram. Soc.*, vol. 72, no. 3, pp. 441–447, Mar. 1989, doi: 10.1111/j.1151-2916.1989.tb06150.x.
[20] B. T. Richards, K. A. Young, F. De Francqueville, S. Sehr, M. R. Begley, and H. N. G. Wadley, “Response of ytterbium disilicate–silicon environmental barrier coatings to thermal cycling in water vapor,” *Acta Mater.*, vol. 106, pp. 1–14, Mar. 2016, doi: 10.1016/j.actamat.2015.12.053.
[21] J. L. Stokes, “β-Cristobalite thermal expansion and stability in environmental barrier coating systems,” *J. Am. Ceram. Soc.*, vol. 108, no. 2, p. e20214, Feb. 2025, doi: 10.1111/jace.20214.
[22] D. Scotson, A. H. Paksoy, and P. Xiao, “Characterisation techniques for investigating TBC and EBC failure: a review,” *Front. Ceram.*, vol. 1, p. 1307437, Jan. 2024, doi: 10.3389/fceic.2023.1307437.
[23] M. Ridley *et al.*, “Steam oxidation and microstructural evolution of rare earth silicate environmental barrier coatings,” *J. Am. Ceram. Soc.*, vol. 106, no. 1, pp. 613–620, Jan. 2023, doi: 10.1111/jace.18769.
[24] S. Yilmaz, M. Theodore, and S. Ozcan, “Silicon carbide fiber manufacturing: Cost and technology,” *Compos. Part B Eng.*, vol. 269, p. 111101, 2024, doi: https://doi.org/10.1016/j.compositesb.2023.111101.
[25] W. R. Haigis and M. A. Pickering, “Monolithic β SiC parts produced by CVD,” *Mater. Des.*, vol. 14, no. 2, pp. 130–132, 1993, doi: https://doi.org/10.1016/0261-3069(93)90007-I.
[26] S. Gobain, “Hexoloy® SA Sintered Silicon Carbide Material,” Saint-Gobain - PERFORMANCE CERAMICS & REFRACTORIES. Accessed: Aug. 03, 2025. [Online]. Available: https://www.ceramicsrefractories.saint-gobain.com/materials/silicon-carbide-sic/hexoloy-silicon-carbide-material/hexoloy-sa-sic-material
[27] R. G. Munro, “Material Properties of a Sintered α-SiC,” *J. Phys. Chem. Ref. Data*, vol. 26, no. 5, pp. 1195–1203, Sep. 1997, doi: 10.1063/1.556000.

[28] N.-L. Zhang, J.-F. Yang, Y.-C. Deng, B. Wang, and P. Yin, “Preparation and properties of reaction bonded silicon carbide (RB-SiC) ceramics with high SiC percentage by two-step sintering using compound carbon sources,” *Ceram. Int.*, vol. 45, no. 12, pp. 15715–15719, Aug. 2019, doi: 10.1016/j.ceramint.2019.04.224.
[29] J. DiCarlo, H.-M. Yun, G. Morscher, and R. Bhatt, “SiC/SiC composites for 1200 C and above,” in *Handbook of ceramic composites*, Springer, 2005, pp. 77–98.
[30] B. Kowalski and B. Harder, “Thermally grown oxide in water vapor on coated and uncoated SiC,” *J. Am. Ceram. Soc.*, vol. 103, no. 10, pp. 5978–5989, Sep. 2020, doi: 10.1111/jace.17295.
[31] D. M. Mieskowski, T. E. Mitchell, and A. H. Heuer, “Bubble Formation in Oxide Scales on SiC,” *J. Am. Ceram. Soc.*, vol. 67, no. 1, Jan. 1984, doi: 10.1111/j.1151-2916.1984.tb19160.x.
[32] N. A. Nasiri, N. Patra, N. Ni, D. D. Jayaseelan, and W. E. Lee, “Oxidation behaviour of SiC/SiC ceramic matrix composites in air,” *J. Eur. Ceram. Soc.*, vol. 36, no. 14, pp. 3293–3302, Nov. 2016, doi: 10.1016/j.jeurceramsoc.2016.05.051.
[33] K. N. Lee, A. Garg, and W. D. Jennings, “Effects of the chemistry of coating and substrate on the steam oxidation kinetics of environmental barrier coatings for ceramic matrix composites,” *J. Eur. Ceram. Soc.*, vol. 41, no. 11, pp. 5675–5685, Sep. 2021, doi: 10.1016/j.jeurceramsoc.2021.04.037.
[34] M. J. Presby, R. M. Sullivan, L. C. Hoffman, B. J. Harder, and K. N. Lee, “Oxidation of an Environmental Barrier Coated Ceramic Matrix Composite in a Combustion Environment,” in *Turbo Expo*, American Society of Mechanical Engineers, 2025, p. V001T02A005.
[35] J. Wan and M. Lipkin, “Articles With Enhanced Temperature Capability,” US 9,969,655 B2, May 2018 [Online]. Available: https://patents.google.com/patent/US9969655B2
[36] K. Luthra, D. Lipkin, and J. Wan, “High Temperature Tolerant Ceramic Matrix Composites and Environmental Barrier Coatings,” US 10,822,998 B2, Nov. 03, 2020 [Online]. Available: https://patents.google.com/patent/US10822998B2
[37] L. R. Turcer and N. P. Padture, “Towards multifunctional thermal environmental barrier coatings (TEBCs) based on rare-earth pyrosilicate solid-solution ceramics,” *Scr. Mater.*, vol. 154, pp. 111–117, Sep. 2018, doi: 10.1016/j.scriptamat.2018.05.032.
[38] S. N. Kabekkodu, A. Dosen, and T. N. Blanton, “PDF-5+: a comprehensive Powder Diffraction File™ for materials characterization,” *Powder Diffr.*, vol. 39, no. 2, pp. 47–59, 2024, doi: 10.1017/S0885715624000150.
[39] Y. F. Su *et al.*, “Quantifying High Temperature Corrosion,” Research Org.: Oak Ridge National Laboratory (ORNL), Oak Ridge, TN (United States), 2021. [Online]. Available: https://www.osti.gov/biblio/1783299
[40] C. A. Schneider, W. S. Rasband, and K. W. Eliceiri, “NIH Image to ImageJ: 25 years of image analysis,” *Nat. Methods*, vol. 9, no. 7, pp. 1–675, Jul. 2012, doi: 10.1038/nmeth.2089.
[41] D. Naumenko, B. Gleeson, E. Wessel, L. Singheiser, and W. Quadakkers, “Correlation between the microstructure, growth mechanism, and growth kinetics of alumina scales on a FeCrAlY alloy,” *Metall. Mater. Trans. A*, vol. 38, no. 12, pp. 2974–2983, 2007.
[42] N. Birks, G. H. Meier, and F. S. Pettit, *Introduction to the High Temperature Oxidation of Metals*, 2nd ed. Cambridge: Cambridge University Press, 2006. doi: 10.1017/CBO9781139163903.

[43] K. Kane, E. Garcia, M. Lance, C. Parker, S. Sampath, and B. Pint, “Accelerated oxidation during 1350°C cycling of ytterbium silicate environmental barrier coatings,” *J. Am. Ceram. Soc.*, vol. 105, no. 4, pp. 2754–2763, Apr. 2022, doi: 10.1111/jace.18231.
[44] B. E. Deal and A. S. Grove, “General Relationship for the Thermal Oxidation of Silicon,” *J. Appl. Phys.*, vol. 36, no. 12, pp. 3770–3778, Dec. 1965, doi: 10.1063/1.1713945.
[45] R. M. Sullivan, “Reformulation of oxide growth equations for oxidation of silicon bond coat in environmental barrier coating systems,” *J. Eur. Ceram. Soc.*, vol. 39, no. 16, pp. 5403–5409, Dec. 2019, doi: 10.1016/j.jeurceramsoc.2019.06.057.
[46] K. N. Lee, J. Stuckner, A. Garg, R. I. Webster, and L. G. Wilson, “Influence of coating variables on the steam oxidation of modified silicon/ytterbium disilicate environmental barrier coatings,” *Surf. Coat. Technol.*, vol. 496, p. 131696, Jan. 2025, doi: 10.1016/j.surfcoat.2024.131696.
[47] R. Sullivan, J. Stuckner, K. Lee, and M. Jaskowiak, “Estimates of Permeability of Water in Rare Earth Silicates Using Modified Theory of Deal and Grove,” National Aeronautics and Space Administration, Glenn Research Center Cleveland, Ohio 44135, E-20082, Jan. 2023.
[48] S. Singh, M. Nganbe, and K. Chen, “Modeling oxygen permeability through topcoat and thermally grown oxide in dense Yb2Si2O7 environmental barrier coatings,” *J. Am. Ceram. Soc.*, vol. 104, no. 12, pp. 6481–6495, Dec. 2021, doi: 10.1111/jace.17996.
[49] D. R. Neuville *et al.*, “Structure Characterizations and Molecular Dynamics Simulations of Melt, Glass, and Glass Fibers,” in *Fiberglass Science and Technology*, H. Li, Ed., Cham: Springer International Publishing, 2021, pp. 89–216. doi: 10.1007/978-3-030-72200-5_2.
[50] W.-J. Lee and Y.-H. Chang, “Growth without Postannealing of Monoclinic VO2 Thin Film by Atomic Layer Deposition Using VCl4 as Precursor,” *Coatings*, vol. 8, no. 12, p. 431, Nov. 2018, doi: 10.3390/coatings8120431.
[51] I. Iatsunskyi, S. Jurga, V. Smyntyna, M. Pavlenko, V. Myndrul, and A. Zaleska, “Raman spectroscopy of nanostructured silicon fabricated by metal-assisted chemical etching,” presented at the SPIE Photonics Europe, C. Gorecki, A. K. Asundi, and W. Osten, Eds., Brussels, Belgium, May 2014, p. 913217. doi: 10.1117/12.2051489.
[52] M. N. Muralidharan, N. C. Pramanik, P. A. Abraham, K. Stanly Jacob, and N. Rani Panicker, “Crystallization and oxidation resistance properties of boron modified silicon oxycarbides derived from polymeric precursors by sol–gel method,” *Mater. Lett.*, vol. 62, no. 17–18, pp. 2547–2550, Jun. 2008, doi: 10.1016/j.matlet.2007.12.044.
[53] T. Narushima, T. Goto, M. Maruyama, H. Arashi, and Y. Iguchi, “Oxidation of Boron Carbide-Silicon Carbide Composite at 1073 to 1773 K,” *Mater. Trans.*, vol. 44, no. 3, pp. 401–406, 2003, doi: 10.2320/matertrans.44.401.
[54] D. Scotson, A. H. Paksoy, E. Yilmaz, and P. Xiao, “Examining the effect of temperature on steam oxidized silicon bond coats,” *J. Am. Ceram. Soc.*, vol. 108, no. 10, p. e20680, Oct. 2025, doi: 10.1111/jace.20680.
[55] J. Rodríguez-Viejo, F. Sibieude, M. T. Clavaguera-Mora, and C. Monty, “18O diffusion through amorphous SiO2 and cristobalite,” *Appl. Phys. Lett.*, vol. 63, no. 14, pp. 1906–1908, Oct. 1993, doi: 10.1063/1.110644.
[56] M. Susa and K. Nagata, “Thermal oxidation of silicon substrates through oxygen diffusion,” *Mater. Sci. Eng. A*, vol. 146, no. 1, pp. 51–62, Oct. 1991, doi: 10.1016/0921-5093(91)90267-Q.

[57] Y. Wang *et al.*, “Dual-feedback healing mechanism redefining anti-oxidation coatings in fiber-reinforced composites,” *J. Adv. Ceram.*, vol. 13, no. 10, pp. 1643–1654, Oct. 2024, doi: 10.26599/JAC.2024.9220966.
[58] N. S. Jacobson, G. N. Morscher, D. R. Bryant, and R. E. Tressler, “High-Temperature Oxidation of Boron Nitride: II, Boron Nitride Layers in Composites,” *J. Am. Ceram. Soc.*, vol. 82, no. 6, pp. 1473–1482, Jun. 1999, doi: 10.1111/j.1151-2916.1999.tb01944.x.
[59] R. C. Breneman and J. W. Halloran, “Stress Development and Fracture of Surface Nucleated Cristobalite on Silica Glass,” *J. Am. Ceram. Soc.*, vol. 97, no. 11, pp. 3483–3488, Nov. 2014, doi: 10.1111/jace.13181.
[60] B. T. Richards and H. N. G. Wadley, “Plasma spray deposition of tri-layer environmental barrier coatings,” *J. Eur. Ceram. Soc.*, vol. 34, no. 12, pp. 3069–3083, Oct. 2014, doi: 10.1016/j.jeurceramsoc.2014.04.027.
[61] R. S. Hay, “Crystallization kinetics for SiO2 formed during SiC fiber oxidation in steam,” *J. Am. Ceram. Soc.*, vol. 102, no. 9, pp. 5587–5602, Sep. 2019, doi: 10.1111/jace.16341.
[62] I. R. Crystal, B. Schauer, E. S. Converse, J. T. Cahill, W. L. Du Frane, and G. C. S. King, “Investigation of B4C for inhibiting crystallization in silica at high temperatures,” *Ceram. Int.*, vol. 50, no. 11, Part A, pp. 19335–19343, Jun. 2024, doi: 10.1016/j.ceramint.2024.03.035.
[63] B. McFarland and E. J. Opila, “Silicon carbide fiber oxidation behavior in the presence of boron nitride,” *J. Am. Ceram. Soc.*, vol. 101, no. 12, pp. 5534–5551, Dec. 2018, doi: 10.1111/jace.15807.
[64] R. Inoue, Y. Arai, Y. Kubota, Y. Kogo, and K. Goto, “Oxidation of ZrB2 and its composites: a review,” *J. Mater. Sci.*, vol. 53, no. 21, pp. 14885–14906, Nov. 2018, doi: 10.1007/s10853-018-2601-0.
[65] M. Futakawa and R. W. Steinbrech, “Viscosity of Amorphous Oxide Scales on SiSiC at Elevated Temperatures,” *J. Am. Ceram. Soc.*, vol. 81, no. 7, pp. 1819–1823, Jul. 1998, doi: 10.1111/j.1151-2916.1998.tb02552.x.
[66] M. N. Muralidharan, N. C. Pramanik, P. A. Abraham, K. Stanly Jacob, and N. Rani Panicker, “Crystallization and oxidation resistance properties of boron modified silicon oxycarbides derived from polymeric precursors by sol–gel method,” *Mater. Lett.*, vol. 62, no. 17–18, pp. 2547–2550, Jun. 2008, doi: 10.1016/j.matlet.2007.12.044.
[67] P. Stack *et al.*, “Dry air cyclic oxidation of mixed Y/Yb disilicate environmental barrier coatings and bare silica formers,” *J. Eur. Ceram. Soc.*, vol. 42, no. 7, pp. 3345–3350, Jul. 2022, doi: 10.1016/j.jeurceramsoc.2022.02.009.